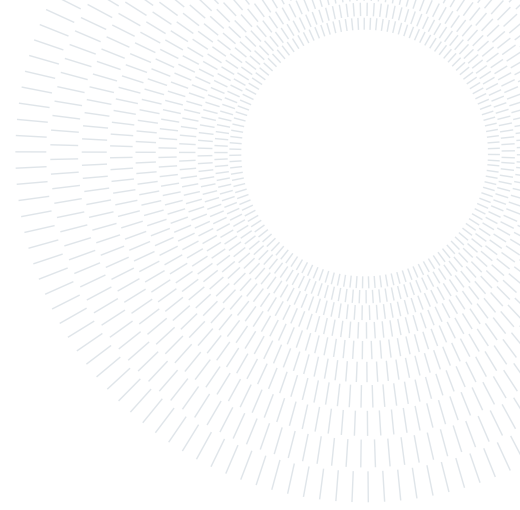




POLITECNICO
MILANO 1863

SCUOLA DI INGEGNERIA INDUSTRIALE
E DELL'INFORMAZIONE



Validation of a CFD simulation of a cavitating hydrofoil with a cryogenic fluid

TESI DI LAUREA MAGISTRALE IN
AERONAUTICAL ENGINEERING - INGEGNERIA AERONAUTICA

Lorenzo Pontello, 10676011

Advisor:
Prof. Federico Piscaglia

Co-advisors:
Jens Honoré Walther
Nicolai Arent Quist

Academic year:
2023-2024

Abstract: Cavitation is a complex phenomenon present in many flows of engineering interest. It represents both a risk (e.g. efficiency losses in turbomachinery) and an opportunity to exploit (e.g. improved fuel injection).

Cavitation is a challenging process to study both experimentally and numerically: it requires advanced instrumentation for the former, while still much empiricism is involved in the models for the latter. This makes the validation of numerical results through experiments compulsory.

In the present work, a brief theoretical introduction is faced. The Schnerr-Sauer method will be used in the VoF framework to deal with multiphase cavitating flow. No thermal effects will be considered.

The object is to perform CFD simulations of the experiment performed by Hord on an hydrofoil immersed in a nitrogen cavitating flow. The numerical simulation activity has been set up as follows.

First, a non cavitating single phase flow is considered as a validation case.

Then, a 2D cavitating flow is simulated: since using a compressible setup has been found to trigger numerical instabilities when CFL is decreased, incompressible fluid properties in saturation conditions are employed. Results are then compared with the experiments and other numerical studies. Inertial controlled cavitation model have been found to underestimate the length of the cavity.

Finally, 3D simulations are carried on considering also a corrective parameter to decrease eddy viscosity inside the cavity in order retrieve possible unsteady effects. Cavity length from 3D computation are found to predict correctly the cavity length and provide better result than 2D for the experiment in exam.

Key-words: Cavitation; CFD; Starccm+; VoF; Multiphase Flow

1. Introduction

Cavitation is defined as the physical process concerning liquid phase vaporization due to local pressure being lower than the saturation pressure. This is a widespread phenomenon observed in many flows of engineering interest. Typical examples are flows in marine propellers and hydrofoils, hydraulic turbines, axial or centrifugal pumps and turbomachinery in general: in all these cases low pressure on the suction side promotes nucleation and vapor bubble growth.

Other less conventional fields where cavitation is observed and studied are the medical industry (such as in heart valve prostheses or ultrasound treatments like histotripsy [19]) or in fuel injection.

Due to its unsteady nature Cavitation is in fact a source of several disruptive behaviors mainly which may result in:

- mechanical erosion caused by collapsing bubble near surfaces. The formation of new crevices on the wall then causes nucleation to increment and feed itself (see heterogeneous nucleation in section 2).
- cavitation noise
- periodic vibrations linked to collapse of bubble clouds, which may cause efficiency losses and interfere with the dynamics of the structures

As anticipated, cavitation can also be exploited in a favorable way in fuel injector: a controlled cavitation in the injector's nozzle can promote the atomization of the fuel mixture that will reach the combustion chamber. Yin et al. [33] found that high pressure injection combined with cavitating flow being injected from a micro-hole nozzle can reduce spray penetration and increase its cone angle, thus favoring an higher quality combustion.

From this brief list of examples one can deduce the importance of studying and investigating this phenomenon in order to develop and employ suitable models. Thanks to the current computational power available, cavitation models can be integrated in CFD code to effectively predict the inception and the development of cavities, beside being a valid aid in design and validation phases of a project.

Achieving this purpose is not trivial, because it requires deep knowledge of the physics, validation through experiments and an important computational effort for numerical simulation. Beside, simulation of cavitation in CFD contains intrinsic criticality that will be discussed in the following section 2.2.

In the present work, the theoretical aspects of cavitation physics and bubble available growth models will be presented in section 2.1: these tools will be used as base material for the numerical simulations.

The report will focus then on the procedure followed to review, analyze and delve into the cavitation mechanism of the flow across an hydrofoil placed inside a wind tunnel. In section 3 the experimental setup based on Hord [7] will be exposed.

The work by Kim et al. [12, 13] has been used as a reference for the general CFD simulation setting: in this way, some of the results can be compared 1:1. The software adopted to perform CFD computations is Starccm+[31] by Siemens.

Section 4 contains the core of the work done: it describes every step followed during the setup of each simulation and critical aspect encountered, as well as the reason behind the choices of all the parameters and methods for each case.

2. Physics and modeling of cavitation

Cavitation originates from liquid being locally in tension ($p < p_{sat}$) allowing tiny vapor impurities (or nuclei) to grow. Literature defines two kinds of formation for nuclei:

- Homogeneous: in this case cavitating bubbles grow from microscopic voids which constitute a negligible volume fraction within the pure liquid domain.
- Heterogeneous: this kind of nucleation originates from small particles in suspension or the interaction of liquid with solid walls (where roughness and crevices play also a major role).

This classification is purely indicative of a different origin, but the two phenomena can happen simultaneously in the same flow producing the same result.

During the initial stage of their growth, bubbles are in equilibrium with the surrounding liquid thanks to surface tension; if $p < p_{sat}$ and cavitation is triggered, the radius of the nuclei start growing.

Cavitating flows are characterized by the cavitation number K_v , which indicates the likelihood of cavitation inception. It is defined as:

$$K_v = \frac{p - p_{sat}}{\frac{1}{2}\rho v^2} \quad (1)$$

2.1. Bubble growth

Several models have been developed to describe the physics and dynamics of a growing bubble: [26] and [24] derived their homonymous class of cavitation model that is here reported in its more complete form (see Brennen [2]).

$$\frac{p_{sat}(T_\infty) - p_\infty}{\rho_L} + \frac{p_{sat}(T_v) - p_{sat}(T_\infty)}{\rho_L} + \frac{p_{v,0}}{\rho_L} \left(\frac{T_v}{T_\infty}\right) \left(\frac{R_0}{R}\right)^3 = R \frac{d^2 R}{dt^2} + \frac{3}{2} \left(\frac{dR}{dt}\right)^2 + \frac{4\nu_L}{R} \frac{dR}{dt} + \frac{2\sigma}{\rho_L R} \quad (2)$$

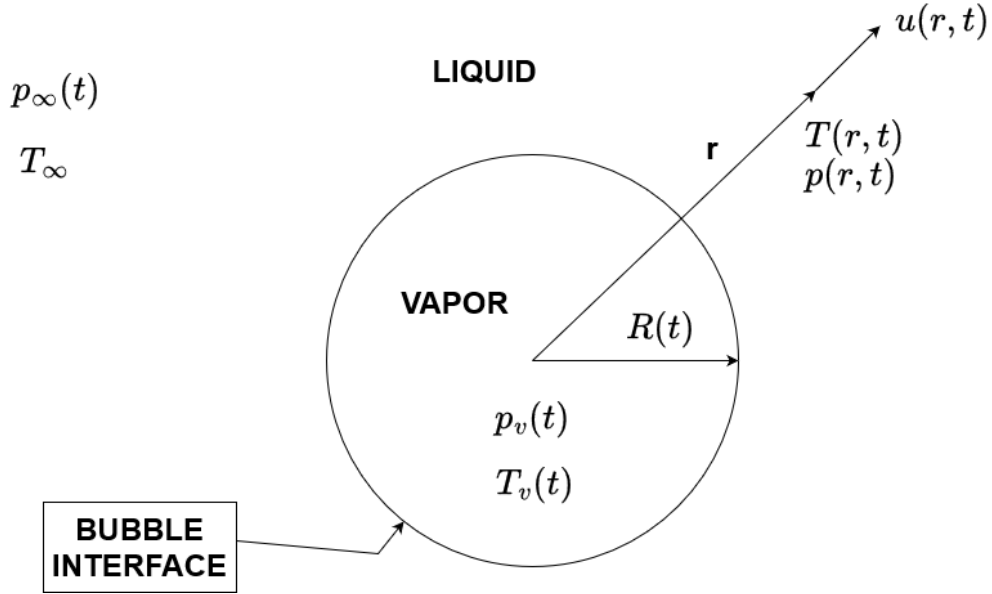


Figure 1: Reference model for bubble growth theory

Equation 2 describes the evolution the radius (R) for a spherical bubble growing in liquid phase such that sketched in figure 1. The far field is characterized by constant asymptotic temperature T_∞ and asymptotic pressure $p_\infty(t)$.

The dynamics of the bubble depends on several parameters such as:

- density of the liquid phase ρ_L
- viscosity of the liquid phase ν_L
- surface tension σ
- temperature of the vapor phase inside the bubble T_v
- initial (seed) radius R_0
- pressure of the vapor inside the bubble at initial conditions $p_{v,0}$

Some approximations can be applied to the model described in equation 2 to distinguish three bubble growth regimes. They are known in literature as surface tension, inertial and thermal controlled regimes according to the dominating term in the equation.

Surface tension-controlled regime As previously stated, at the initial instants the bubble radius is almost constant and the equilibrium with the liquid phase is set by surface tension. For instance, Kim [13] uses this observation to employ the Young-Laplace and model the minimum radius of the bubble nuclei (or seeds):

$$R_0 = \frac{2\sigma}{p_{sat} - p} \quad (3)$$

Inertial controlled regime The inertial controlled regime is an approximation in which the thermal effects are neglected: the liquid temperature is considered uniform and the second rhs term in equation 2 is null. With this assumption the original model for the growth rate by Rayleigh-Plesset is finally retrieved:

$$\frac{dR}{dt}_i = \sqrt{\frac{2}{3} \frac{p_{sat} - p}{\rho_L}} \quad (4)$$

This expression also neglects the presence of bubble growth acceleration, viscous effects, and surface tension effects as they are considered of minor importance when compared to the liquid inertia.

This behavior is observed after liquid inertia prevails over surface tension making the bubble grow. In this stage, the growth rate is therefore modeled as constant (see Lien [18]).

Thermal controlled regime Thermal effects will now be considered in the case where the bubble is surrounded by a uniformly superheated liquid at T_∞ , such that $T_v \neq T_\infty$. Under the hypothesis of thin bubble interface compared to bubble radius, Plesset and Zwick [23] suggested a relation between temperature difference $T_v - T_\infty$ and bubble growth rate:

$$\frac{dR}{dt} = \sqrt{\frac{3 D_L}{\pi t_b}} Ja \quad (5)$$

where Jacob number is defined as the excess of energy per unit of liquid volume relative to the energy required to form the unit volume of vapor[18]:

$$Ja = \frac{\rho_L C_{pL} (T_\infty - T_v)}{\rho_v L} \quad (6)$$

This growth rate has been found to match with the experiments (Lien [18], Kosky[14]) when the bubble growth time exceeds a critical time defined as:

$$t_c = \frac{p_{sat} - p_\infty}{\rho_L \Sigma^2} \quad (7)$$

where Σ is a thermophysical quantity that depends both on asymptotic temperature T_∞ and material properties:

$$\Sigma = \frac{\rho_v^2 L^2}{\rho_L^2 C_{pL} T_\infty \sqrt{D_L}} \quad (8)$$

From the physical point of view, this happens because temperature of the liquid in contact with the vapor interface is limited on the lower bound by the saturation temperature. During the growing process this temperature difference decreases up to the point where diffusive thermal energy across the bubble interface becomes the limiting factor to its radius growth.

This translates in the second lhs term (thermal) of equation 2 being dominant with respect to the other. This is actually a gradual process, and an intermediate regime can be defined between inertial and thermal controlled growth. Mikic et al. [20] defined a global function for $R(t)$ which encompasses all cavitation regimes (see figure 2) except for lower radius values in surface tension controlled regime.

Two final remarks need to be made.

First, this dissertation about physical modeling contains several simplifications as many contributions have been neglected (i.e. effects of thermal non-equilibrium, convection, mass diffusion, thermodynamic stability). Similarly, bubble collapse (although important, see section 1) won't be treated or modeled. Section 2.2 contains the details of how condensation has been treated in the computational framework.

The second important point is the following: whether thermal effects have to be taken into consideration or not depends on how the growing time of bubble for the specific set of operative conditions of the flow compares to its critical time t_c (equation 7). If $t < t_{ch}$, an inertial growth regime model like equation 4 can be applied, while if $t > t_{ch}$ thermal effects are dominating the bubble radius growth velocity is properly approximated by equation 5.

For the cases considered in the present work (see section 3) the correct model to adopt for cavitation should comprehend thermal effect, since the critical time for nitrogen (as for cryogenic fluids in general) is quite low (about $2 \cdot 10^{-7}$ s according to Kim [13]) and therefore it is easily exceeded by the time that cavitation bubbles develop. Despite that, in the implementations of numerical simulations the bubble grow rate model will not take into account thermal effects, basically neglecting the cooling effect due to vaporization.

The bubble growth rate is computed locally using equation 4 as implemented in Starccm+ and defined in its user guide [30]. The following section will expose more details on the computational aspects of the model.

2.2. Numerical implementation of the cavitation model

Volume of Fluid method CFD simulation will be conducted via Starccm+ software by Siemens. Finite Volume Method (see Peric [3]) is the adopted approach for the discretization of the domain and the governing equations. the solution is achieved by means of a segregated solver that compute each discretized governing equation in a sequential manner, iterating until convergence is obtained.

To solve the cavitating problem, an eulerian-approach for the multiphase solver is adopted. Specifically, a Volume of Fluid (VoF) method is employed. This technique has been first applied by Nichols and Hirt [21], and then gained popularity for solving problems involving free surface interface capturing (i.e. see [6]).

VoF belongs to the family of single fluid model: only one set of governing equations is solved for both phases. This avoids the high computational cost of two fluid model (eulerian-eulerian approach) which requires to solve one set of governing equation per phase (or fluid) that need to be coupled at the interface.

In VoF method each cell is characterized by the volume fraction α_i of each phase, which corresponds to the relative volume occupied by said component of the mixture. For the i-th phase, the volume fraction is defined as:

Experimental Data (Superheat, System pressure, Jakob #)	
▲	1. Dergarabedian(1960), water, 0.8 °C, 1 atm, Ja=2.37
◆	2. Dergarabedian(1960),Methanol, 6.4 °C,1 atm,Ja=9.2
✕	3. Florschuetz(1969), water, 3.61 °C, 1 atm, Ja=10.77
○	4. Lien(1969), water, 9.0 °C, 0.381 atm, Ja=65.28
+	5. Kosky(1968), water, 36 °C, 0.488 atm, Ja=207.68
-	6. Lien(1969), water, 10.67 °C, 0.124 atm, Ja=217.47
□	7. Bohrer(1973), R113, 34.1 °C, 0.084 atm, Ja=425.79
◇	8. Bohrer(1973), R113, 48.2 °C, 0.036 atm, Ja=1237.51
△	9. Lien(1969), water, 15.74 °C, 0.012 atm, Ja=2750.66
—	Equation of Mikic et al (1970)
- - - -	Equation of Rayleigh (1917), (Inertia)
- - - -	Equation of Plesset & Zwick (1954), (Diffusion)

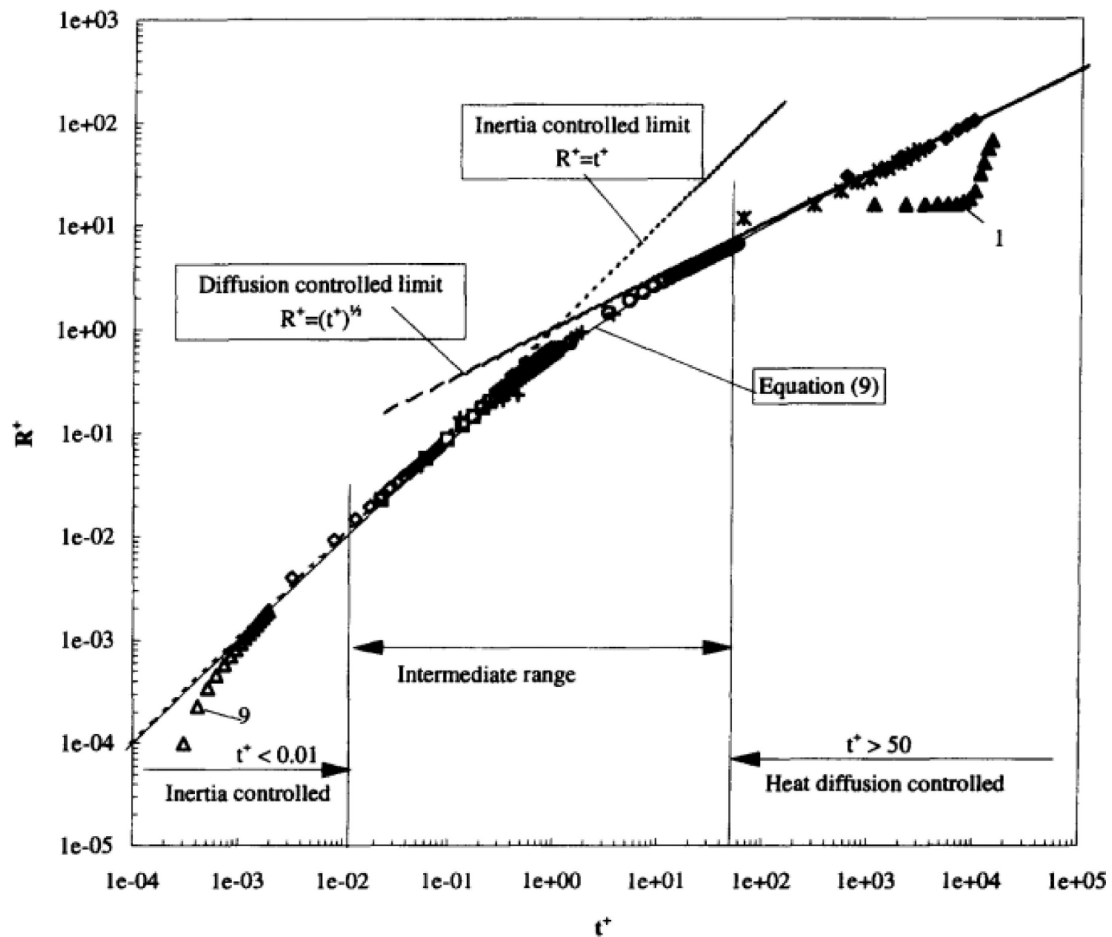


Figure 2: Normalized bubble radius vs normalized time; comparison between experimental data and three analytical models: Rayleigh (inertial range), Plesset&Zwick (thermal range) and Mikic. Figure from Lee and Merte [16]

$$\alpha_i = \frac{V_i}{V} \quad (9)$$

such that it sums up to unity:

$$\sum_{i=1}^n \alpha_i = 1 \quad (10)$$

Volume fractions for the $n - 1$ phases (the last one is obtained by difference) become then a set of additional primitive variable that needs to be computed solving for an equal number of governing equation, here reported in a generic conservative differential form:

$$\frac{\partial \alpha_i}{\partial t} + \nabla \cdot (\alpha_i \mathbf{U}) = S_i \quad (11)$$

It should be highlighted that any slip velocity among phases' interface is neglected.

In VoF, each cell is associated with a unique value for density, velocity, temperature and pressure. In order to make it possible for a multiphase flow, the contribution of the material properties from each phase is weighted as follows:

$$\rho = \sum_{i=1}^n \rho_i \alpha_i \quad (12)$$

$$\nu = \sum_{i=1}^n \nu_i \alpha_i \quad (13)$$

$$Cp = \sum_{i=1}^n \frac{Cp_i \rho_i}{\rho} \alpha_i \quad (14)$$

$$\lambda = \sum_{i=1}^n \lambda_i \alpha_i \quad (15)$$

$$(16)$$

Cavitation model integration with VoF The next important remark regards the source term S_i , and how VoF (originally thought to assess free surface problems) has been adapted to deal with cavitation.

Since resolving the free surface of each cavitating bubble would require an excessive mesh resolution for the case of interest, VoF is employed to build a sub grid model for cavitation that computes just the volume occupied by bubbles in each cell. This is explained in greater detail by Schnerr and Sauer [28].

The inertial controlled growth rate derived by Rayleigh and Plesset for a single bubble (see equation 4) is incorporated into the source terms of the volume fraction governing equation 11.

In a two-phase flow such that of the experiment of interest (see section 3) only one volume fraction equation is solved (usually the one for vapor phase). Its source term is the volume flux transfer among phases inside the cell and it is split into two contributions: vaporization (positive) and condensation (negative).

This model is based also on the hypothesis of an homogeneous distribution of N perfectly spherical nuclei (or seeds) with the same initial radius R_{min} in the fluid domain of volume V . The seed density is then defined as:

$$\eta = \frac{N}{V} \quad (17)$$

This parameter plays a major role in the accuracy of the results, as it directly affects the source term of vapor production (or dissolution). This can be observed in the following equation for the source term of vapor phase:

$$S_v = 3\alpha_v \left(\frac{4\pi(1 - \alpha_v)\eta}{3\alpha_v} \right)^{\frac{1}{3}} \frac{dR}{dt} \quad (18)$$

where the term $\frac{dR}{dt}$ is the same expressed in equation 4 for the inertial regime (this model has been proposed by Schnerr and Sauer [29]).

It is worth summarizing some criticality of the present setup, pointing out possible corrective directives from literature:

- The term $\frac{dR}{dt}$ is computed explicitly using quantities from the previous iteration. This poses a strong constrain on the CFL condition necessary to converge to a stable solution.

For instance, in the unsteady simulation presented from section 4.3 going on, the time step for temporal discretization has been computed imposing a Courant number of 0.3. This is a stricter condition whereas

$CFL < 1$ is generally suggested (see also StarCCM+ user guide [30]). This has been done in order to stabilize even more the solution as an equivalent way of reducing the under-relaxation factors.

- The cavitation model assumes an homogeneous value for both seed density and initial radius of the nuclei. This poses two problems: first, the actual spatial distribution of the nuclei is not homogeneous; second, its number is not known a priori and it's different for every flow. For this reason, a lot of empiricism is involved in the choice and tuning of this parameters. There are two ways to assess the issue: the first being adding a supplementary transport equation for η as done by De Giorgi et al. [4] and described by Kim et al. [12]; the second is to consider two different non-uniform seed density field for condensation and vaporization that depend on other parameters (as done by Kim et al. [13]).

3. Experimental setup of reference

Comparing results obtained through numerical simulation with experiments is a fundamental step to establish the accuracy of the computation. Given the wide range of error sources (e.g. discretization and round off error) and empiricism involved in models (e.g. for turbulence and cavitation) raw data are basically meaningless by themselves.

CFD analysis in the present report simulate the experiment conducted by Hord[7]. The numerical solutions will be compared then to experimental measures to assess the quality of their setup.

The experimental procedure consists in a cryogenic liquid flowing through a test tunnel where a symmetric tapered hydrofoil is placed at zero degree angle of attack. The experimental campaign carried on involves pressure and temperature measurements from the surface of the hydrofoil. The overall uncertainty for temperature measures is $\pm 0.2K$, while for pressure is $\pm 0.69N/cm^2$.

For a complete description of the test facility (comprehensive of the tunnel, the support for the hydrofoil and the power plant) refer to Hord[7, 8].

The hydrofoil geometry features a circular leading edge of 3.175 mm; its chord is 63.5 mm long and is 25.4 mm wide along the span wise direction (see figure 3).

Several experiments have been conducted for various velocity, pressure and temperature values imposed at the tunnel inlet section. In this way data for different of far-field cavitation numbers $K_{v,\infty}$ have been collected. Simulations of non cavitating cases has also been performed (see section 4.2).

The choice of simulating this specific flow comes from the fact that CFD analysis of Hord's experiment is extremely widespread in literature, therefore lot of data from other numerical simulations are available. Among the others, Kim et al.[13] will be used as a reference for 2d simulations in section 4.3. Other publications considered for a comparing results are Tseng et al. [32], Hosangadi et al. [9] and Goel et al. [5].

One critical aspect to consider in this experiment is the scarce number of data available from measurements (5 temperature and 5 pressure measures). This limitation is due to the technological constrain in fitting the probes available at the time in an hydrofoil of modest dimensions.

Furthermore, the probes are located in positions such that they cannot effectively capture neither the depression peak on the leading edge nor the pressure increase corresponding to a cavity tail.

Figure 4 shows some pictures of the cavitation occurring on the hydrofoil during the experiments. There is no clear link between pictures and experiments' IDs but, judging by cavity length, none of the photos depict the cavitating flow simulated in sections 4.3 and 4.4.1.

4. Numerical implementations

This section deals with the description of the setup for the simulated cases and their results.

The procedure followed involves the simulation and validation of increasingly more complex cases in order to assess their robustness and, in the meantime, identify possible weaknesses.

The first case is a simple simulation of a 2d, single phase, non cavitating flow of liquid nitrogen performed to compare the pressure coefficient's distribution on the hydrofoil surface with experiments and data obtained by Kim[13].

Then cavitation is introduced considering the Schnerr-Sauer model (see [29]) for bubble growth, which is already implemented in Starccm+.

Finally, 3d simulations are carried on in order to verify the presence of three-dimensional effects and the influence of turbulence modeling on prediction of unsteady phenomena.

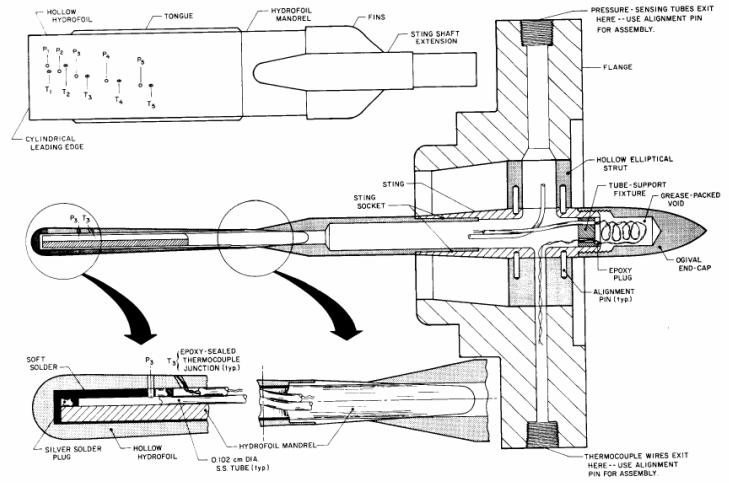
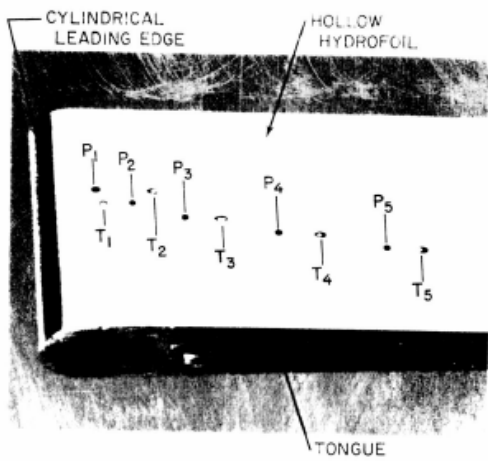


Figure 3: Experimental setup: on the left, the hydrofoil with the probes' positions for temperature and pressure measures; on the right, the complete assembly with the support.

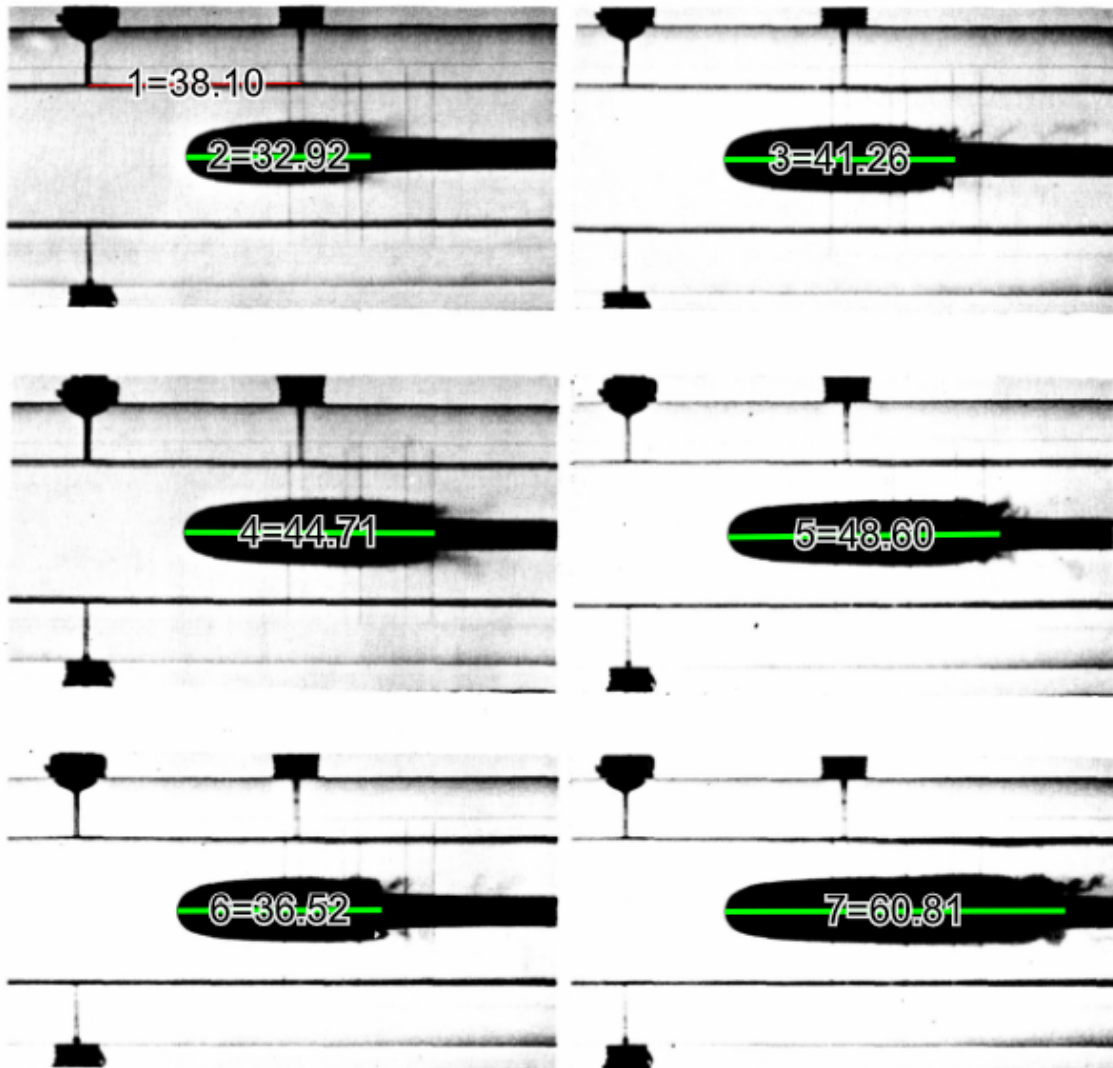


Figure 4: Pictures of some cavities developed on the hydrofoil during the experiments. Dimensions are in millimeters

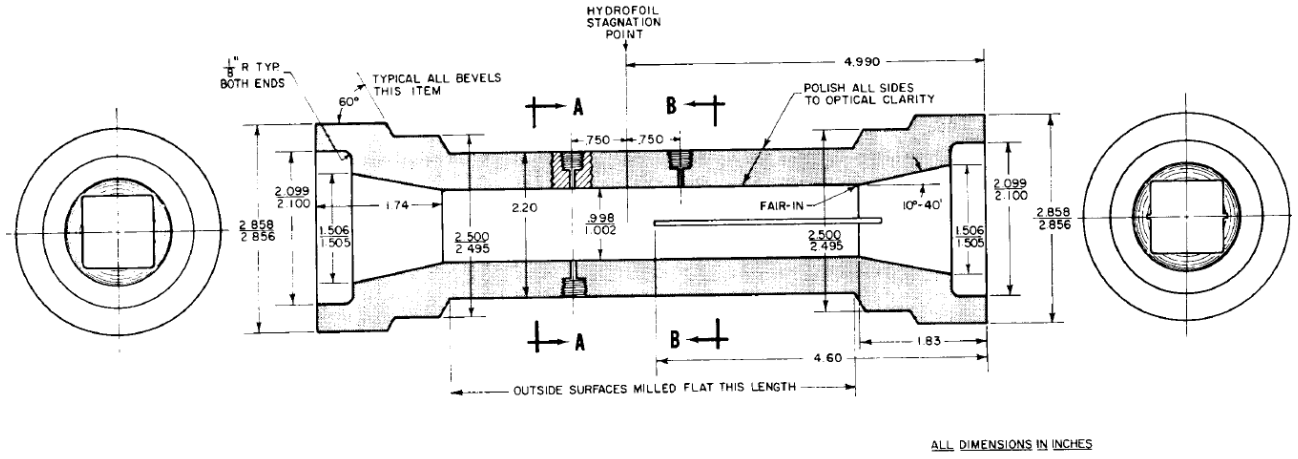


Figure 5: Section of test tunnel used by Hord (dimensions in inches) and sketch of the geometry for the present computational domain (dimensions in millimeters)

4.1. Source of modeling error

Experimental data are necessary to validate numerical results, which are affected by errors intrinsic to the adopted models. Some of the sources from which they arise are reviewed in the following paragraphs.

Geometry of the domain The computational domain considered is just a subset of the entire test tunnel: in particular, convergent and divergent sections at the extremes were neglected, as well as the presence of the hydrofoil's support. This simplifies the geometry without losing accuracy in the region of interest, where the cavity is expected to develop and grow from the hydrofoil's leading edge. Figure 5 shows the geometry chosen for the simulation and a section of the experimental wind tunnel.

The geometry is assumed to be perfectly symmetric along the horizontal plane. Because the flow is expected to be symmetric too, only half of the domain has been considered: this allows to save computational resources as halves the dimension of the domain.

Computational grid Numerical computation requires spatial discretization, which means that the domain needs to be divided in smaller volumes constituting the mesh. In the finite volume framework it is required that each quantity is computed at the cell center node and it is assumed to be homogeneous inside each cell volume. Clearly the higher the mesh resolution, the more accurate the computed fields (especially where large gradients occur).

The mesh in exam is characterized by large density gradients in the cavity region as well as high velocity gradients near the wall where the non-slip condition is imposed.

For this reason each mesh employed for the present simulations have been refined in those area.

Boundary conditions Choosing the right set of boundary conditions is fundamental to represent accurately the physical properties and converging to and meaningful solution. In the present case, quantities at the inlet section were made available in [7] available for each test case, while at the outlet the mass flow rate was imposed.

Two approximations have been made for the model:

1. **Adiabatic walls for both the tunnel and hydrofoil surfaces:** perfect thermal isolation of the walls is assumed. Clearly, this is not the case especially when operating fluids at very low temperature as those

involved in this experiments. Nonetheless, this hypothesis keeps the simulation from becoming overly complicated. Besides, modeling heat transfer with the external environment is beyond the goal of this work as it would rely on too many variables.

2. **Smooth wall surface:** again, this is an idealization given that real surfaces cannot be perfectly smooth. Roughness leads to consequences on both near wall turbulence and on nucleation. The first requires the modification of the log-law[25], although much empiricism is involved in this tuning operation. The second is the heterogeneous nucleation generated from wall crevices (see Brennen [2]), but the localized concentration of nuclei has been already dismissed in the assumption of homogeneity made for the cavitation model in section 2.2.

Fluid properties Multi-phase cavitating flows such those considered in the present report are characterized by fluid properties that depend on both pressure and temperature, therefore a fully compressible model should be adopted (as in [13]). On the other hand, other studies employ temperature dependent properties (see [9], [5], [17]).

In the following sections this aspect will be analyzed and different models will be considered in order to optimize the computational effort, the accuracy of the solution and its numerical stability.

Turbulence model and 2d approximation Two dimensional flow model has been assumed to be appropriate as first approximation. This simplification allows simulations to be less computationally expensive and delivers acceptable results provided the aspect ratio of the hydrofoil is large enough. In this way the results can be used to directly compare solutions from other 2d simulations (e.g. [13], [32], [9], [5]) in a consistent manner. On the other hand, turbulence is a three dimensional phenomenon which could impair the accuracy of the results. As stated by Perić[22], 2d RANS simulations provide reliable only for statistically steady flows: this is the case for a flow where the cavity is fully developed and attached to the surface. Conversely, only 3D LES or DES simulations can provide results which reflect the experiments and capture effectively the unsteady phenomena.

4.2. Case 1: non cavitating case

The first case analyzed is a non cavitating one. The flow is single phase (liquid nitrogen).

This simulation is carried out to check if the basic aspects of the simulation are correctly chosen and set up (i.e. geometry, mesh, boundary conditions, fluid property, solvers' parameters, post processing routines).

C_p distribution along the hydrofoil wall will be compared with both the experimental measures and the numerical solution obtained by Kim [13].

4.2.1 Simulation setup

Hord [7] does not specify from which test condition the results on non cavitating case have been taken. As a matter of fact, pressure coefficient's distribution for Euler flows does not depend on the asymptotic reference pressure p_{in} , but only on the geometry of the hydrofoil. For this reason, comparing pressure coefficients' values with the experiment is also an opportunity to verify the fidelity of the hydrofoil's geometry with respect to the real one.

However, when viscous effects are considered, the value for $C_{p,min}$ and its position along the hydrofoil surface also depend on the Reynolds number (and so on the inlet velocity v_{in}). For this reason, two cases with different cavitation number ($K_{v,\infty}$) have been arbitrarily selected to be simulated (specifically case 289D and 292A, designated by Hord as of "*desinent cavitation*").

Measured quantities at the tunnel inlet section are reported in table 1.

Mesh A mesh of 231936 cells has been generated (see figure 6). Grid resolution has been refined around the leading edge where cavitation is supposed to take place. Prism layers have been generated to improve resolution near the walls where velocity gradients are larger. In this way, the same mesh can be employed also for the cavitating cases presented afterwards.

The maximum skewness angle is 45.59 deg and all cells have both face validity and maximum volume change in range $[0.1 \div 1]$. Overall there are 68683 quadrilateral cells and 163253 polygonal cells.

Boundary conditions The boundary condition imposed at the inlet is of type `Stagnation inlet`, where total pressure is computed from quantities defined in table 1:

$$p_{tot} = p_{in} + \frac{1}{2}\rho_{in}v_{in}^2 \quad (19)$$

	289D	292A	Units
v_0	21.4	9.3	[m/s]
T_0	88.67	76.56	[K]
p_0	743.9	158.3	[kPa]
K_v	2.46	1.89	[-]
α_L	1	1	[-]
α_v	0	0	[-]

Table 1: Inlet quantities for cases 289D and 292A

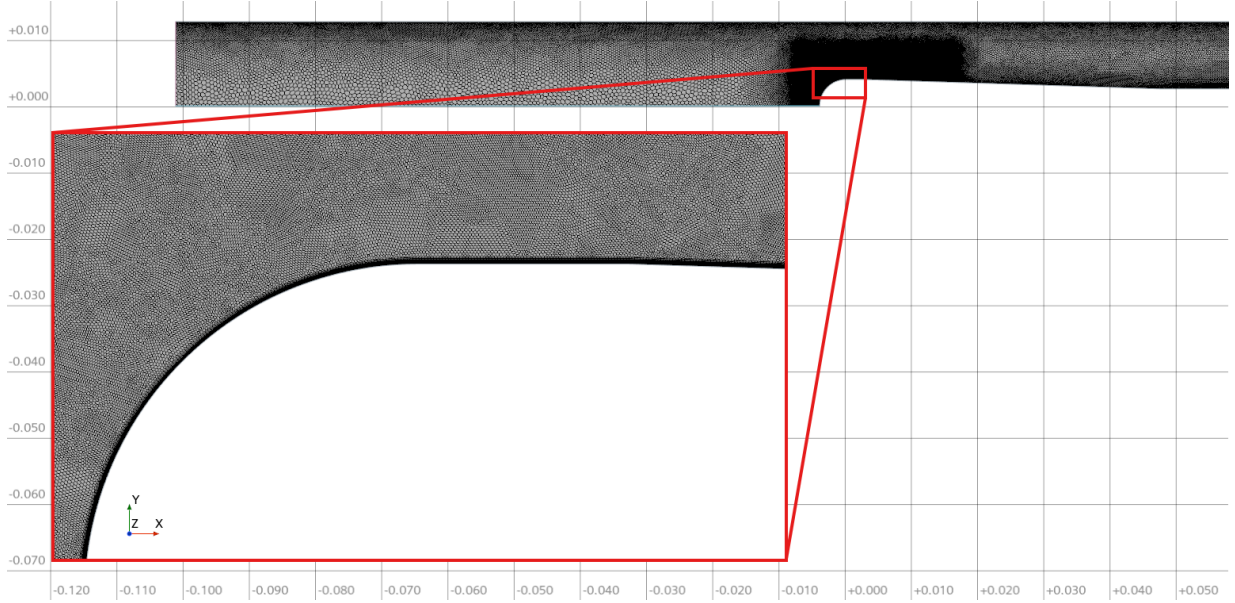


Figure 6: Computational grid used for the present computation (231936 cells) with detailed view of the refined area

and inlet density is defined as function of T_{in} in saturation condition:

$$\rho_{in} = \rho(T_{in}) \Big|_{sat} \quad (20)$$

Turbulent quantities are based on length scale of 7% of the inlet height (h) and turbulence intensity of 5%. These quantities haven been chosen from a reasonable range of values for this kind of flows.

At the outlet, a boundary condition of type `Outlet` was used. There, the mass flow rate per unit of length is set as:

$$\dot{m}_{out} = \dot{m}_{in} = \rho_{in} v_{in} h \quad (21)$$

The values of mass flow rate for non cavitating flows analyzed here are summarized in table 2.

The other boundaries are the hydrofoil and tunnel's wall set as type `wall` (where no-slip and adiabatic conditions are imposed) and the plane of symmetry where a boundary of type `Symmetry Plane` is used.

	289D	292A	Units
\dot{m}_{out}	204	95.6	$\left[\frac{\text{kg}}{\text{m}\cdot\text{s}} \right]$

Table 2: Outlet quantities for cases 289D and 292A

Variable	Factor	AMG cycle	Acceleration
Pressure	0.3	v cycle	Bi Conjugate Gradient Stabilized
Velocity	0.7	Flex cycle	[-]
Energy	0.5	v cycle	[-]
Turbulence	0.5	Flex cycle	[-]

Table 3: Under-relaxation factors and solver parameters

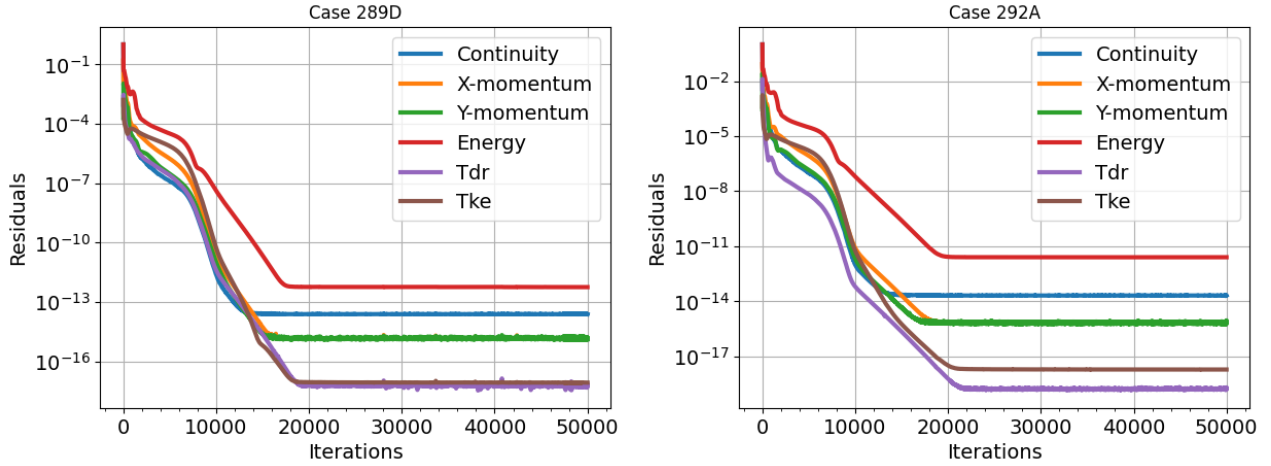


Figure 7: Residuals for case 289D and 292A

Turbulence model The adopted RANS turbulence model is realizable $k - \epsilon$ with *two layer-all* y^+ wall treatment, which provides more stable solution for this specific case rather than $k - \omega SST$. The latter model will be applied for cavitating simulations.

Material properties Temperature dependent properties for density, viscosity, specific heat and thermal conductivity of nitrogen have been set in saturation conditions. It can be argued that, for such a low speed liquid, an isothermermal approximation with constant properties could fit as well. However, this has been chosen to be established as an *a posteriori* test. Material properties were taken from Cool Prop database [1].

Solvers, methods and schemes Due to the lack of cavitation or other unsteady phenomena in general, a steady segregated solver was used to speed up the computation towards the solution. Segregated temperature solver was also set up to solve for the energy equation. Convecting schemes for both solver are II order accurate, as well as that for gradient discretization (II order Venkatakrishnan scheme). Solution for the linearized equations are performed through Algebraic Multigrid method (AMG) with Gauss-Seidel relaxation scheme. Constant (No Ramp) under-relaxation factors have been employed according to table 3 to augment the stability of the solution.

Initial conditions Homogeneous fields have been used to initialize the simulation. Their values are those at the inlet section, but for pressure (it was set such that $p_{init} < p_{in}$ in order to promote convergence, in particular 0.5 MPa for case 289D and 0.1 MPa for case 292A).

4.2.2 Results

Convergence The simulations of non cavitating cases have quickly converged: residual plots (figure 7) show that a steady solution is reached in about 22000 iterations for both cases. Figure 10, 11 and 12 indicate that other monitored quantities (namely minimum/maximum pressure and vertical component of the hydrodynamic force) line up on their asymptotic value after just 2000 iteration.

Figure 8 and 9 show that boundary conditions for pressure and velocity are correctly set at the inlet where they are imposed).

Boundary conditions for mass flow rate (imposed at the outlet) are also verified for both case 289D:

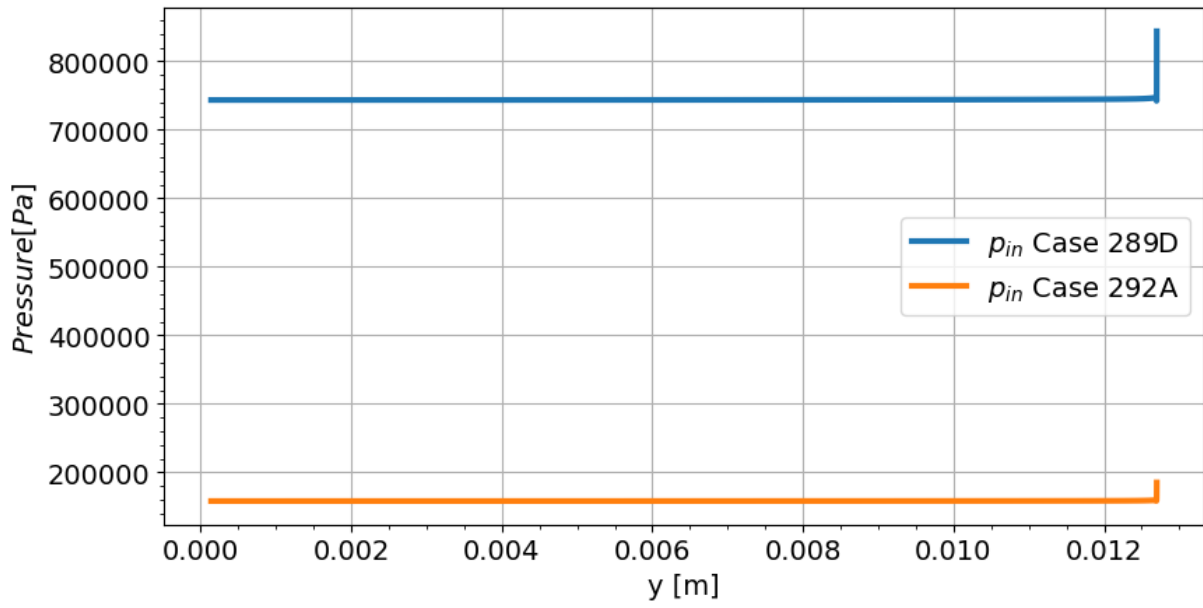


Figure 8: Pressure boundary conditions along y direction for converged solutions

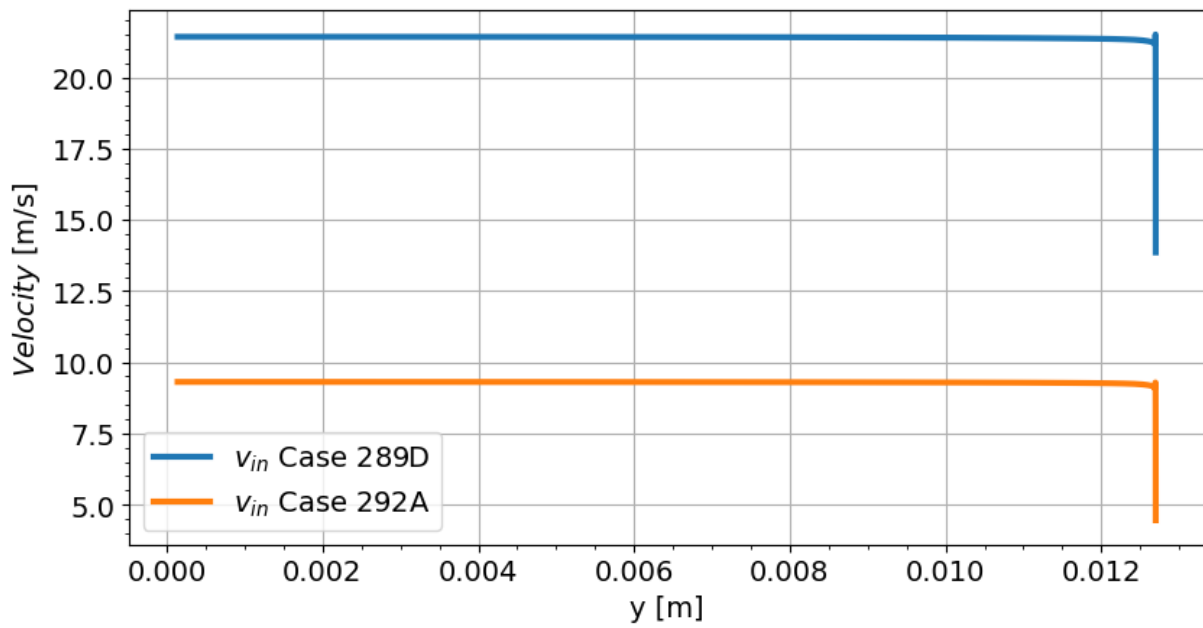


Figure 9: Velocity boundary conditions along y direction for converged solutions

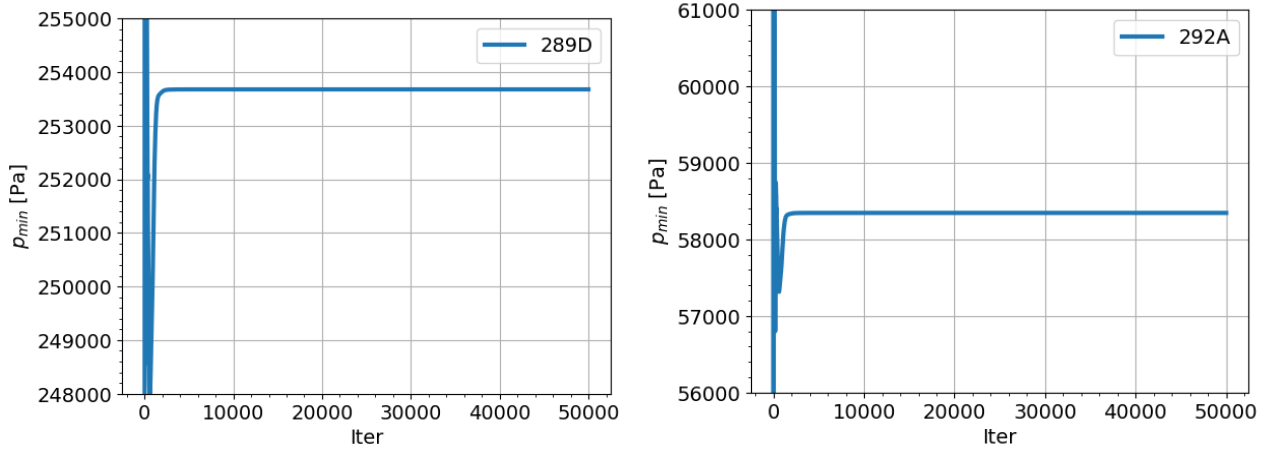


Figure 10: Minimum pressure vs iterations

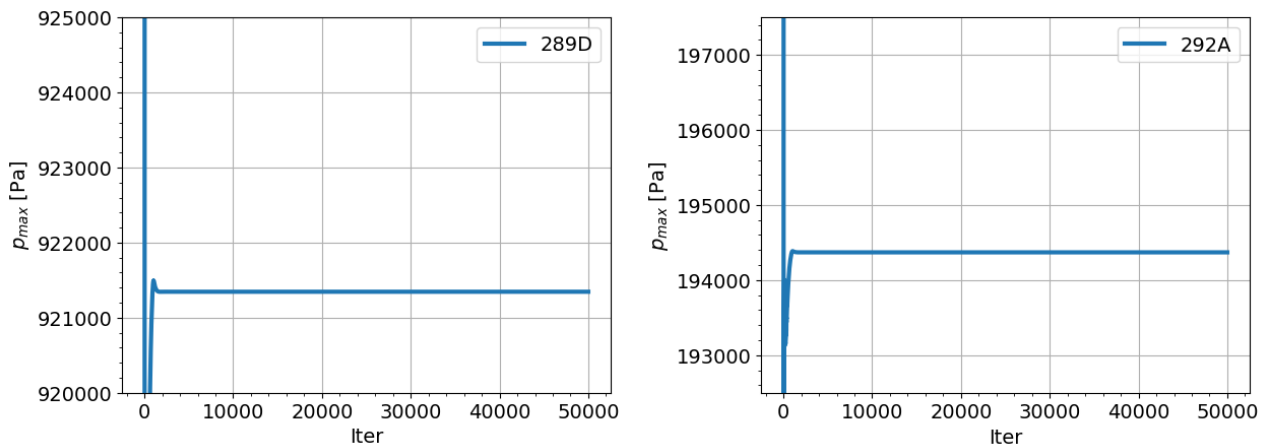


Figure 11: Maximum pressure vs iterations

Part	Value (kg/s)
-----	-----
fluidDomain: Inlet	-2.043700e+02
fluidDomain: Outlet	2.043700e+02
-----	-----
Total:	-5.684342e-14

and case 292A:

Part	Value (kg/s)
-----	-----
fluidDomain: Inlet	-9.560000e+01
fluidDomain: Outlet	9.560000e+01
-----	-----
Total:	0.000000e+00

In both simulations the net value is within machine error limit.

Validation Temperature and density fields for both solution are practically uniform, confirming the hypothesis that an isothermal constant density approximation could have been successfully applied. Temperature and density range value are summarized in table 4.

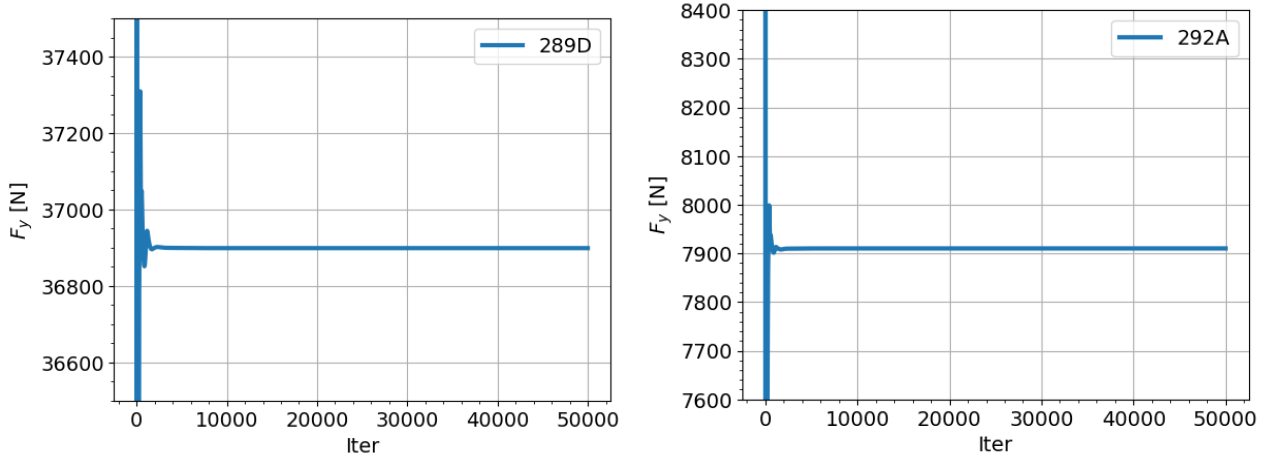


Figure 12: Hydrofoil vertical force vs iterations

Case	Density	Temperature
289D	750 ÷ 752 kg/m ³	88.7 ÷ 89 K
292A	809 ÷ 810 kg/m ³	76.6 ÷ 76.7 K

Table 4: Range values of temperature and density fields for cases 289D and 292A

Pressure coefficient The pressure coefficient is defined as:

$$C_p = \frac{p - p_{in}}{\frac{1}{2}\rho_{in}v_{in}^2} \quad (22)$$

Figure 13 displays values of pressure coefficient on the hydrofoil surface : as a reference, the abscissa for $x = 0$ refers to the center of the leading edge’s osculating circle.

Figure 13 shows that all numerical data series are (almost) perfectly overlapped (except in the rear region toward the outlet, where the difference is negligible though).

Experimental data are reasonably close to the simulations. As anticipated in section 3, no measure is available near the leading edge, which makes it impossible to compare the real value and position of the pressure coefficient’s minimum peak.

In his paper Hord [7] provides also numerically computed results provided by a finite difference code (see [10, 11]) to complement experimental values. Table 5 contains computed data for C_p^{min} and their position along the longitudinal axis.

Results for the single phase setup herein tested show that the geometry of the domain is valid to model adequately the 2d domain. Boundary conditions are correctly set to produce a consistent and converged solution as well. To conclude, this configuration can be reasonably applied as a starting point for the cavitating case setup.

Dataset	C_p^{min}	Position [m]
Hord [7]	-2.88	$-8.30 \cdot 10^{-4}$
Kim [13]	-2.85	$-8.96 \cdot 10^{-4}$
Present (289D)	-2.85	$-8.67 \cdot 10^{-4}$
Present (292A)	-2.86	$-8.67 \cdot 10^{-4}$

Table 5: Pressure coefficients computed peaks and their position

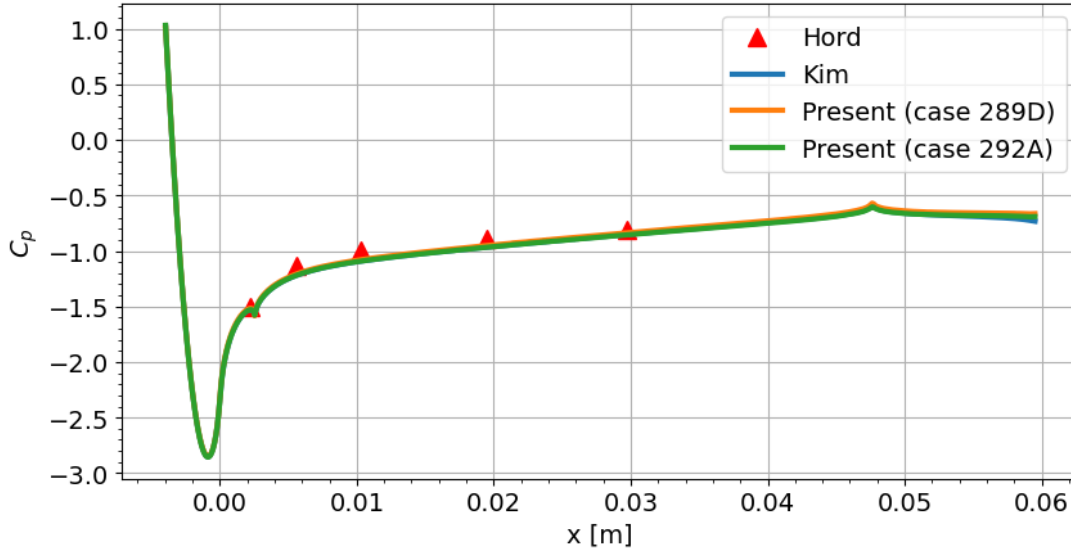


Figure 13: Pressure coefficient on hydrofoil surface for non-cavitating case. Comparison among experimental data, Kim [13], and present computation of cases 289D and 292A

4.3. Case 2: 2d cavitating flows

In this section cavitation is introduced, therefore a multiphase VoF model for volume fraction capturing is needed. As anticipated, only inertial controlled growth regime model is considered. Schnerr-Sauer method (see [28, 29]) is already natively implemented in Starccm+ so that results can be directly verified with experimental measures and numerical data from other studies that use the different models.

Another key aspect to consider is that an unsteady solver is needed. In fact, cavitation is an inherently unsteady phenomenon and time discretization requires particular care due to the stiff source term in the volume fraction transport equation. On the other hand the experiment conducted by Hord does not specify any indication of time, therefore it is reasonable to suppose that a cavity develops and grows along the hydrofoil chord during a transient period of time after which it gets to a steady solution. This scenario is compatible with the application of a RANS turbulent model, although further observation will be addressed in section 4.4.1.

In order to verify this behavior, all the simulations have been carried on for about 20 ms, corresponding to 7 flow through times.

Three configurations have been prepared and will be presented in the current section, as each of them is characterized by different fluid properties. First, a fully compressible case has been proposed in order to get a model as realistic as possible (fully compressible fluid properties are also considered in [12, 13]). Later on it was observed that his setup suffers numerical instability (see section 4.3.2) when CFL number is decreased. Therefore, other configurations have been considered: inspired by other studies (see [5, 9, 32]) constant density has been imposed for liquid phase. Vapor phase has temperature-dependent density in saturation conditions insted.

4.3.1 Simulation setup

The experimental case considered for the simulation is 290C from [7]. Experimental data about the inlet quantities are reported in table 6.

The mesh used is the same as the one shown in figure 6. The boundary condition's type are also the same described in section 4.2. Values for turbulent boundary conditions are still the same as they are defined by means of a length scale and turbulent intensity, because they are linked to the geometry of the inlet and independent on the cavitation mechanism.

Parameters used to set up the solvers are again the same of table 3. This time the `seggregated` solver is unsteady implicit based on SIMPLE algorithm (see [3]). The time step is adapted to the CFL condition: further comments and analysis on this particular aspect will follow in section 4.3.2. Also a segregated VOF solver is added: under-relaxation of 0.9 has been set with a v cycle for AMG and Gauss-Seidel relaxation scheme. This time $k - \omega SST$ will be used with *low* y^+ wall treatment (which requires $y^+ < 1$) in order to be consistent with the model employed in studies used for comparing results (in particular Kim [12, 13]).

Cavitation model parameters Schnerr-Sauer model (see equation 18) requires two parameters to work:

Quantities	Value	Units
v_0	23.9	[m/s]
T_0	83.06	[K]
p_0	568.3	[kPa]
$K_{v,\infty}$	1.7	[-]
\dot{m}_{out}	236	[kg/(m·s)]

Table 6: Inlet quantities for case 290C

Case ID	ρ_L	ρ_v	Other Properties	CFL
A	$\rho_L(p, T)$	$\rho_v(p, T)$	$f(p, T)$	0.5
B	<i>const</i>	$\rho_v(T)$	$f(p, T)$	0.3
C	<i>const</i>	$\rho_v(T)$	$f(T)$	0.3

Table 7: Recap table for the analyzed 2D cases

1. D_0 : is the initial diameter of soon-to-grow bubble and corresponds to the dimension of a seed. It has been set to $1 \cdot 10^{-6}$ m.
2. η : is the homogeneous seed density. Typical order of magnitudes for this parameter are $10^5 \div 10^9$ bubbles/m³ for cryogenes or 10^{13} bubbles/m³ for water according to Kim[13]. In order to allow for a 1:1 comparison with to their simulation, the value of $\eta = 10^9$ bubbles/m³ has been used.

Material properties Three configurations for fluid properties will be employed, in particular:

1. **Case A**: fully compressible, all properties for both phases depend on local pressure and temperature according to tabular value from coolprop database [1].
2. **Case B**: liquid phase has constant density computed such that:

$$\rho_{liq} = \rho(T_{in})|_{sat} = 780 \frac{\text{kg}}{\text{m}^3} \quad (23)$$

while specific heat is temperature dependent (along the saturation line) and other quantities (dynamic viscosity and thermal conductivity) are both pressure and temperature dependent. Vapor phase is fully compressible, and its density depend on both local temperature and pressure.

3. **Case C**: density of the liquid is the same as for case B, but this time vapor and liquid phase properties depend on local temperature only (as in saturation condition).

Table 7 summarizes the main feature of fluid properties that characterize each case; in following sections these IDs are used to identify them.

Initial conditions The flow fields have been initialized with the steady state solution from a precursor run featuring an incompressible single phase (liquid) flow set using the same boundary conditions of the present cases.

4.3.2 Results

After $t = 0.02s$ the cavity is fully developed and it is no more growing: its position is stable for all cases, as observed in the experiments by Hord and in other computations (see [5, 9, 13, 32]).

Benchmark data The only common ground upon which is possible to perform a quantitative comparison of all (experimental and numerical) results are pressure and temperature data on the hydrofoil surface. In particular, the reference parameter for pressure is Δp_{surf} , measured in $\frac{N}{cm^2}$ is defined as:

$$\Delta p_{surf} = \frac{p - p_{sat,\infty}}{10000} \quad (24)$$

where $p_{sat,\infty}$ is a constant value equal to the saturation pressure corresponding to the inlet temperature.

Time discretization, CFL condition and numerical instabilities Originally the 2d simulation was set up to be compressible and the time step such that $CFL = 0.5$. The results obtained in this way are those referred in the following paragraphs as *case A*.

In a subsequent attempt to improve the stability and accuracy of the solution, the CFL has been reduced to 0.3. As soon as the Courant number is set to values lower than 0.5, instability and inconsistency in the solution fields (specifically for pressure) is observed. Specifically, the pressure field experiences periodic oscillations near the leading edge of the hydrofoil: the fact that pressure values there lay on their lower limit (set to $1000Pa$) clearly indicates that this behavior is non-physical and linked to numerical instabilities which eventually lead to the divergence of the solution. In appendix 6, a sequence of images for the pressure field is shown in detail. This finding is counterintuitive: decreasing the time step should, as a matter of fact, increase stability and accuracy of the computation improving convergence. Here, on the other, numerical instabilities are arising. One possible explanation is that the pressure-velocity coupling is less strong for a compressible solver (especially for very low mach number such that involved in this specific case) which results in stiffer convergence rate. At the same time, the density gradients involved in the cavity region are quite high: this may cause some error to propagate due to a lower time step not being able to diffuse it. This can explain the oscillations in the spurious pressure field.

For this reason it was decided to adopt incompressible fluid properties and two configurations have been realized (i.e. case B and C). As already stated at the beginning of section 4.3, this is an acceptable approximation as many other studies have been carried on using variables in saturation conditions. Case B has been selected as an hybrid configuration to test the dependence of pressure on other fluid properties, such as viscosity or specific heat.

Analysis of the results Figures 14 and 15 show a comparison among results obtained in the present simulations, those reported by Kim and the experimental measures by Hord.

Regarding pressure data, figure 14 displays a reasonable behavior for all the simulations. In particular, case A is closer to the first two pressure values near the leading edge than Kim's results. On the other hand, only case C computes correctly the pressure near the third probe. Finally, all three simulation provide similar results outside the cavity region (characterized by $\Delta p_{sat,\infty} < 0$) and are closer to the experiment rather than Kim's.

The cavity position and length (measured by Hord as 1.90 cm long) is approximately given in figure 14 where $\Delta p_{sat,\infty} < 0$. None of the cases predict it correctly (mostly due to the cavitation model not considering thermal effects as stated in [13]). On the other hand, there are just not enough experimental data to correctly capture the actual pressure distribution and its step-like increase near cavity tail's position. For this reason, case C could be considered as the one providing the most correct approximation of the experimental measures. One peculiar aspect to notice is the difference in the minimum $\Delta p_{sat,\infty}$: all present cases showcase a peak which is higher in absolute terms than Kim's, somehow predicting larger vaporization near the leading edge. This is a common behavior of the present study's results regardless of the compressibility effects being considered or not; other studies reveal similar results (see Tseng [32] and Goel [5] in figure 22).

For what concerns surface temperature, clearly case C with Kim's results perform better than the other two configuration, with the compressible case largely over predicting the temperature inside the cavity. In general, all the simulations considered cannot provide satisfactory results for surface temperature. Again, this is most likely due to the limitation of the inertial controlled growth rate model that is characterized by sudden condensation in the cavity tail, thus leading to a considerable increment of the local temperature barely outside the cavity region.

Figure 16 shows the vapor volume fraction plot of the cavity region (isocontour for $\alpha_v = 0.25$), while figure 17 shows the isocontours of the three cases overlapped on the same domain background for $\alpha_v = 0.25$. The compressible case exhibits a different shape, more compact in the y direction. Unfortunately, there are no useful experimental evidences to compare it against, so it is not possible to tell which model predicts the cavity profile the better.

Figures 18, 19, 20 and 21 display pressure, velocity magnitude, temperature and density flow field solutions respectively for cases A, B and C. Their appearance clearly resembles the general shape of the respected cavity, as expected.

Comparing the three configurations, further comments can be made: first, the instabilities occurring when CFL is lowered for the compressible case (A) is a limiting factor to consider when choosing this model (although it provides promising results especially near the leading edge pressure field). Second, computational effort deserves a mention: clearly interpolating fluid properties in two variables (temperature and pressure) is much more demanding than considering temperature dependent quantities in saturation conditions. This performance deficit is quantified in elapsed time per iteration of case B being more than double of case C (0.16s against 0.07s). Results for case B are also the farthest from the experiment and its predicted cavity length is the shortest: for these reasons the configuration and setup of case C is chosen as baseline for further investigations in three dimensions.

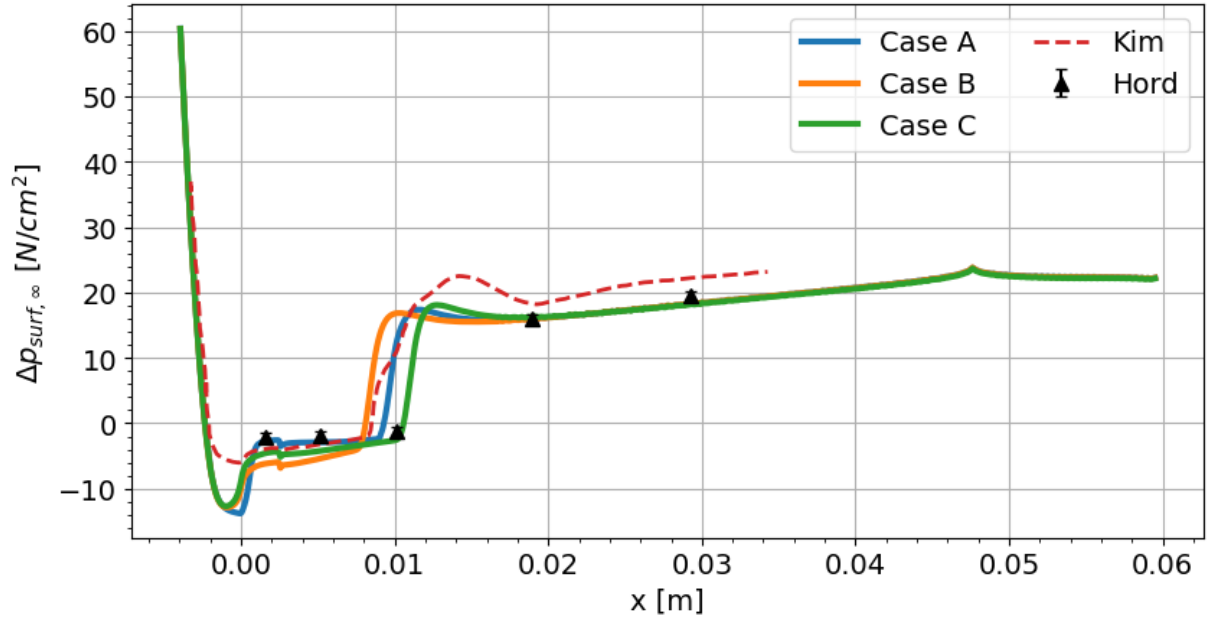


Figure 14: Surface pressure depression of present computations vs experiments and Kim's numerical results

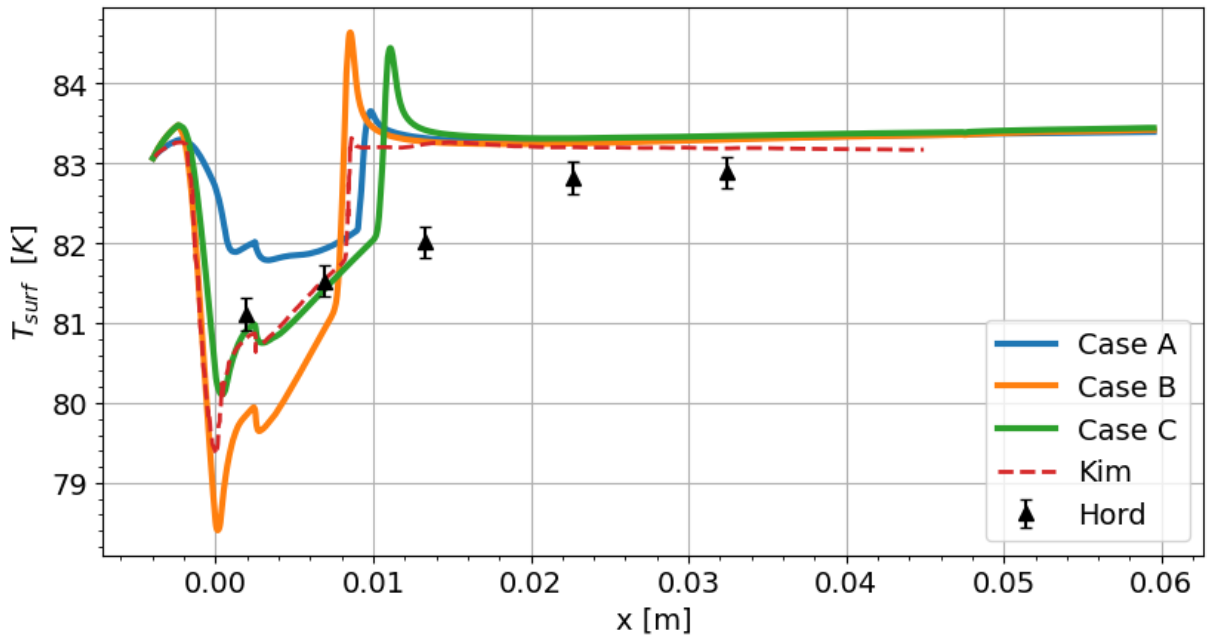


Figure 15: Surface temperature of present computations vs experiments and Kim's numerical results

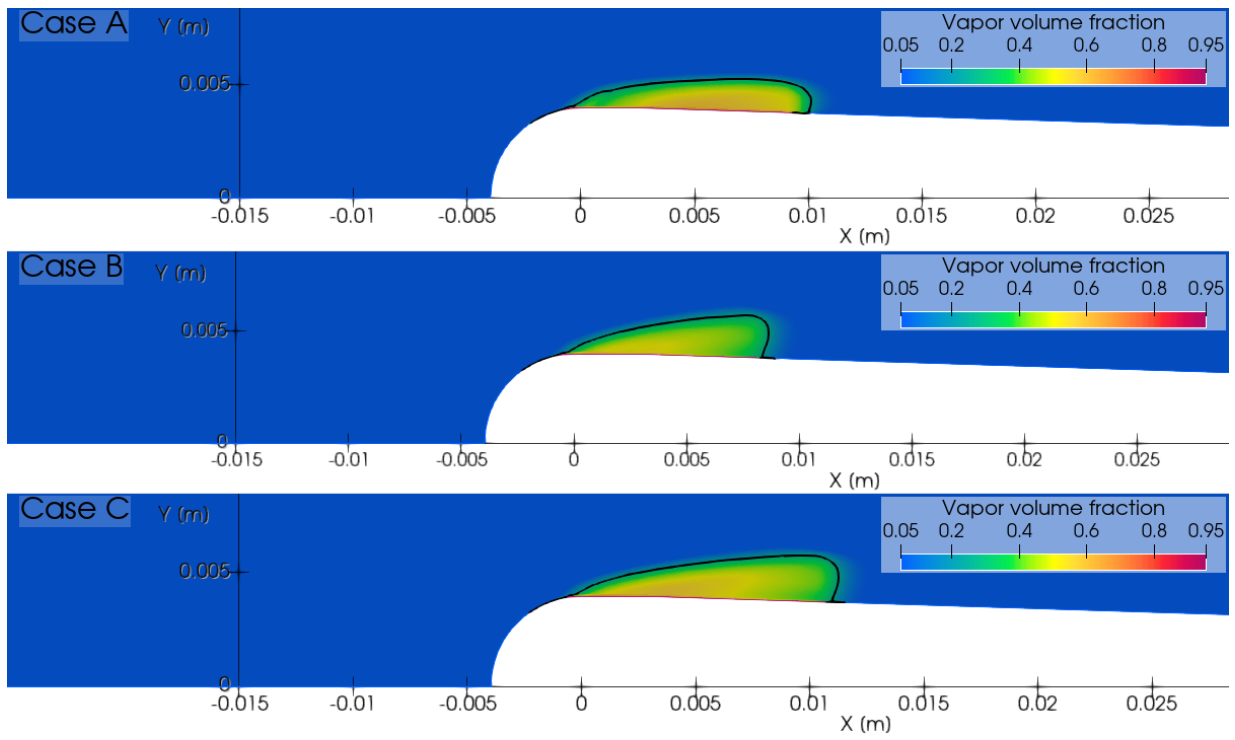


Figure 16: volume fraction for vapor phase (isocontour for $\alpha_v = 0.25$)

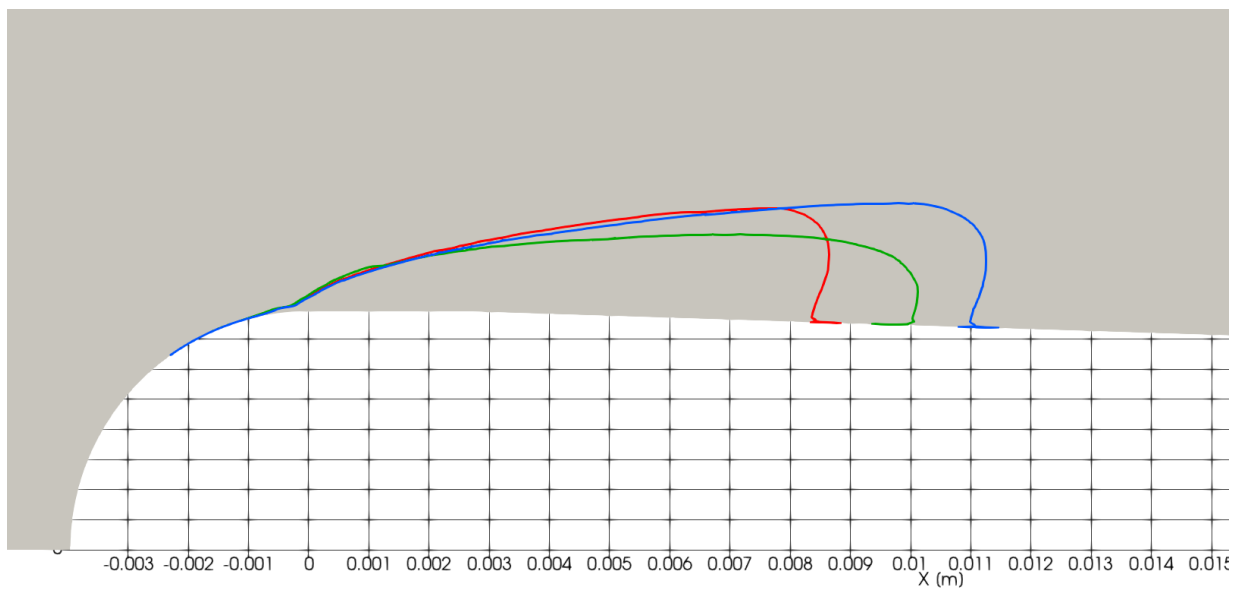


Figure 17: Isocontour for $\alpha_v = 0.25$ of case A (green line), case B (red line) and case C (blue line)

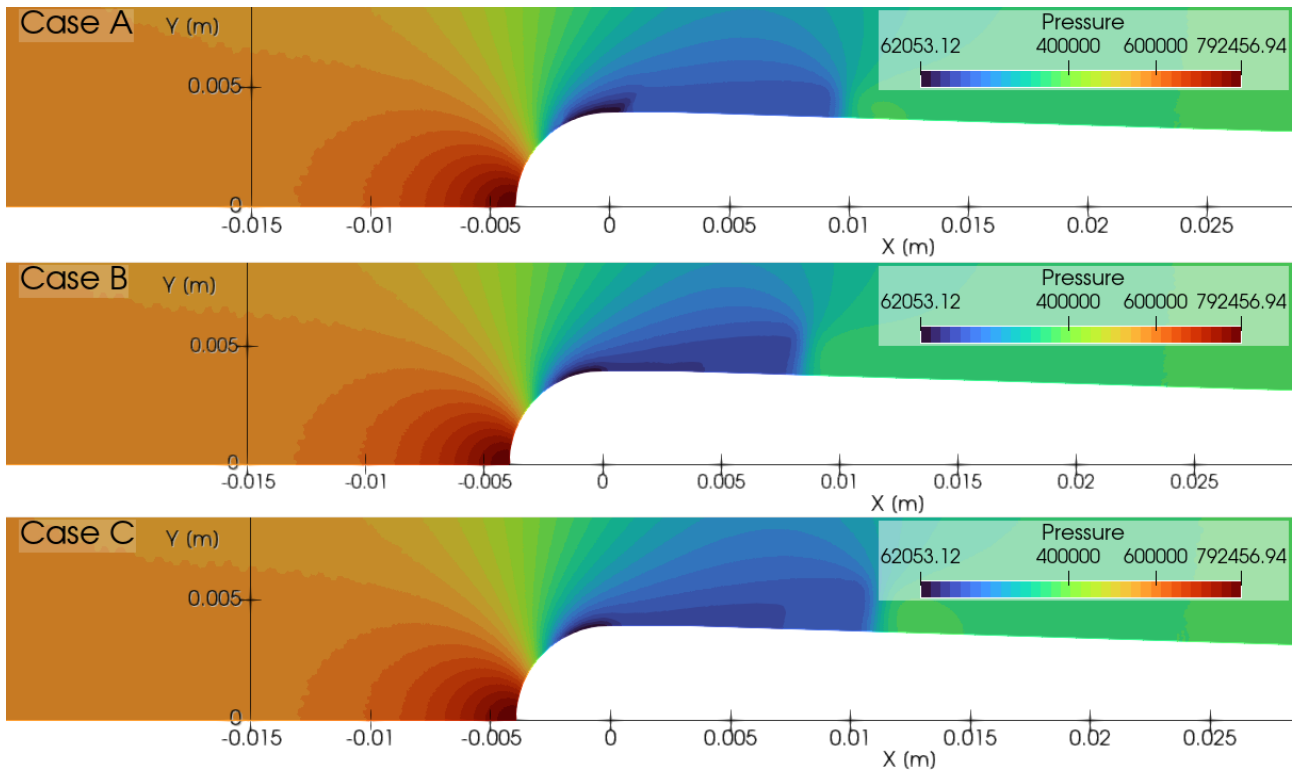


Figure 18: pressure fields

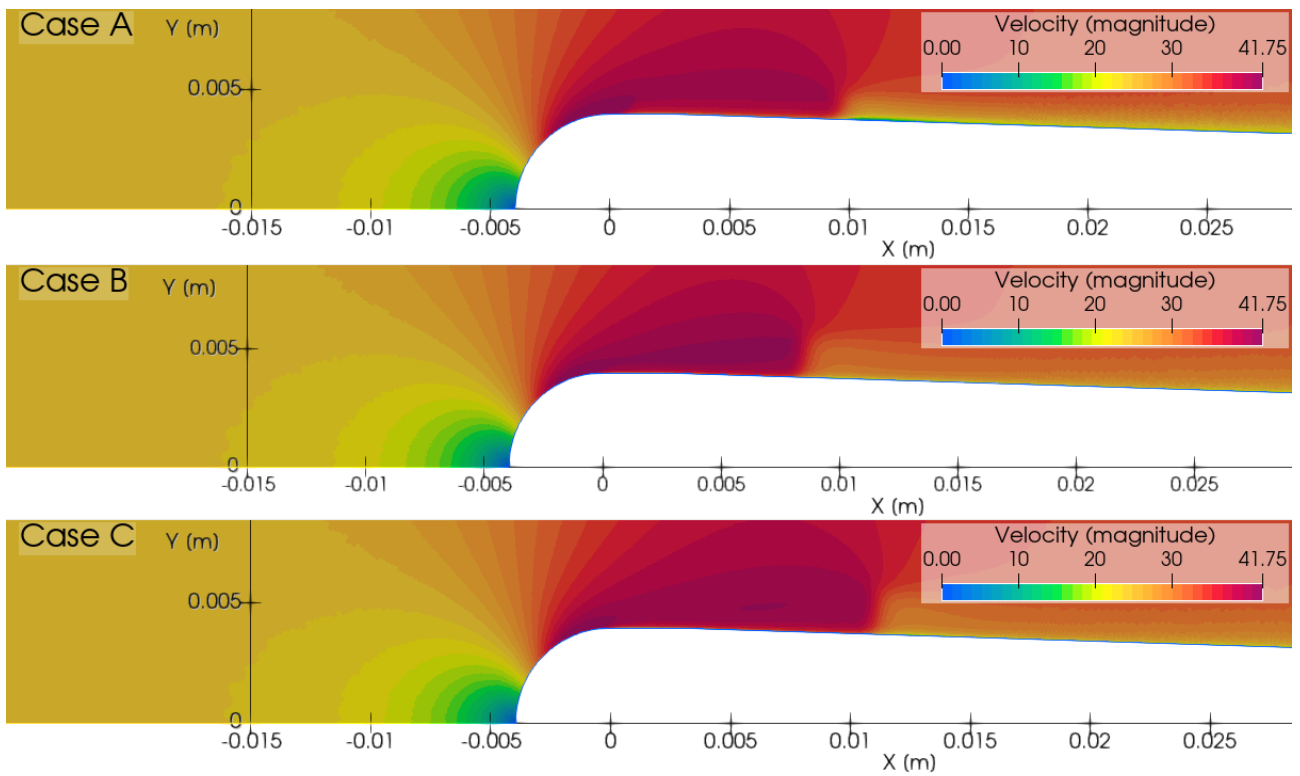


Figure 19: velocity magnitude fields

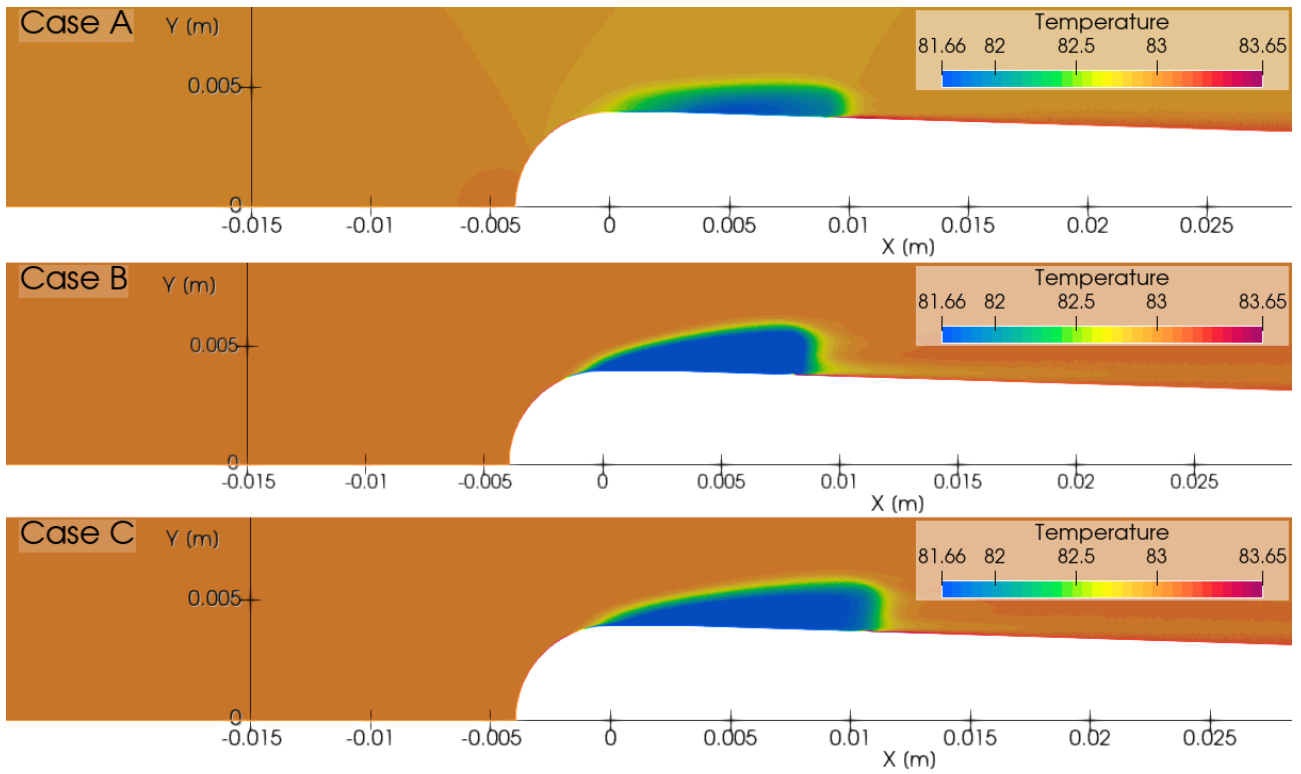


Figure 20: temperature fields

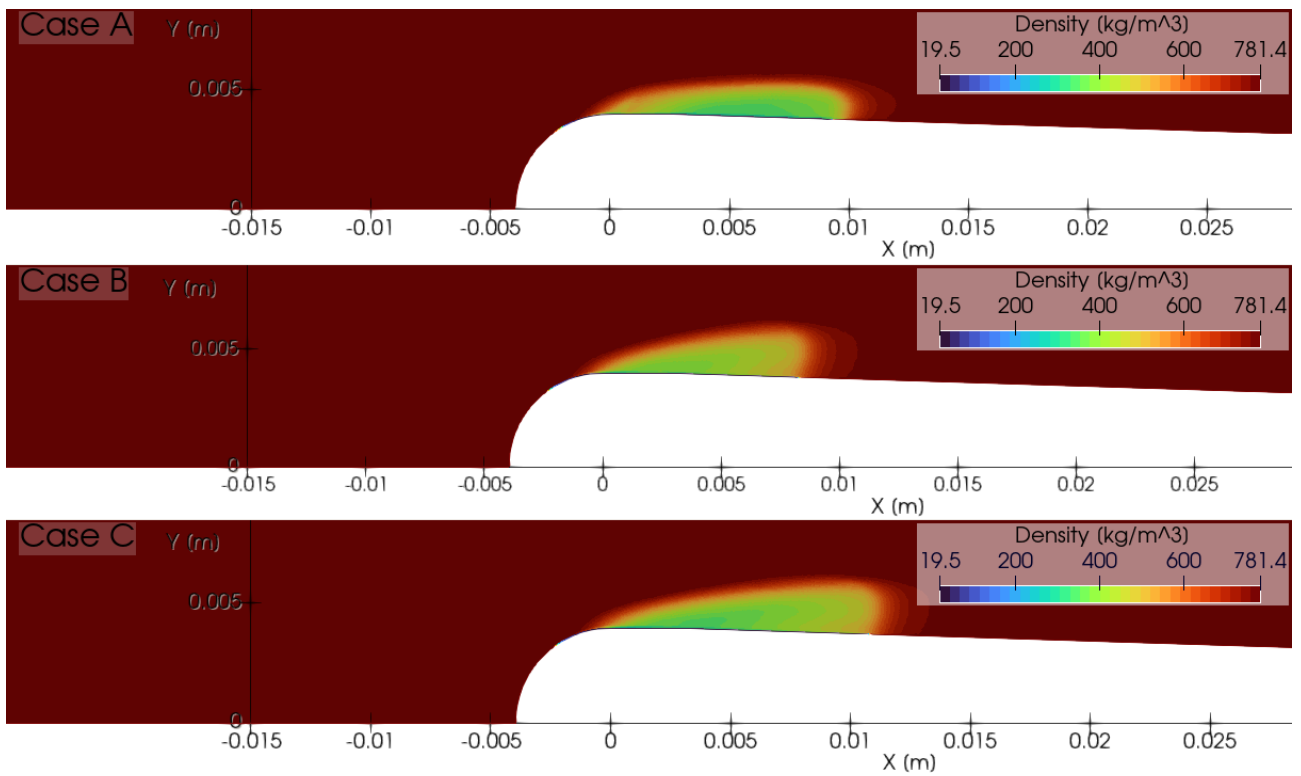


Figure 21: mixture density fields

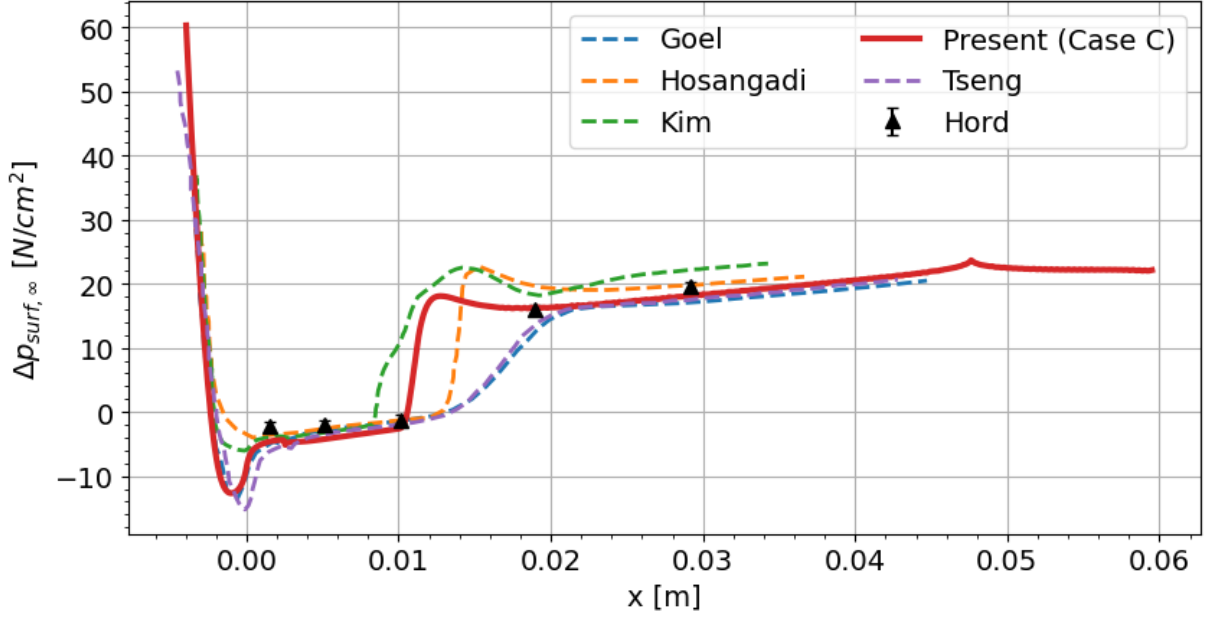


Figure 22: Surface pressure depression of Case C vs experiments and numerical results from Kim and other studies Goel [5], Tseng [32], Hosangadi [9]

Parameter	Regular mesh	Refined mesh
Number of cells	231936	696152
Base size	$5 \cdot 10^{-4}$ m	$2.5 \cdot 10^{-4}$ m
Target size	$1.25 \cdot 10^{-4}$ m (25%)	$6.25 \cdot 10^{-5}$ m (25%)
Minimum cell size	$3.5 \cdot 10^{-4}$ m (7%)	$1.75 \cdot 10^{-5}$ m (7%)
Growth rate	1.05	1.05
Prism layer total thickness	$8 \cdot 10^{-5}$ m	$8 \cdot 10^{-5}$ m
Layer near wall thickness	$1 \cdot 10^{-7}$ m	$8 \cdot 10^{-7}$ m
Number of layers	30	30
Refinement box cell size	$3.5 \cdot 10^{-4}$ m (7%)	$1.75 \cdot 10^{-5}$ m (7%)

Table 8: Mesh setup parameters for both *regular* and *refined* configurations. Dimensions relative to base size in parenthesis ()

Before concluding this section, case C results are compared with those of other studies in figures 22 and 23.

Mesh independence check Finally, a check for mesh independence is lead using case C as the baseline configuration. A simulation is run on a refined grid generated imposing the parameters summarized in table 8 and displayed in figure 24.

Figure 25 shows instead values of y^+ along the wall of the tunnel and the hydrofoil surface (the x axis of the reference system is the same of all the other plots). Given that the prism layer settings are the same, the two data series are similar and the values are everywhere lower than 1 but in a region near the leading edge where it is barely exceeding unity.

Figure 26 reports the comparison of the results obtained on the two grids. A slight difference in the cavity's tail position can be appreciated, otherwise the two curves for surface temperature and $\Delta p_{sat,\infty}$ are perfectly overlapping.

4.4. Case 3: 3d cavitating flows, RANS

Given the prominent role that turbulence plays in cavitation, it is natural to focus on this particular aspect while trying to increase the fidelity of the model.

Turbulence is a three dimensional phenomenon, in the sense that even if the mean flow is 2d, turbulent fluctuation

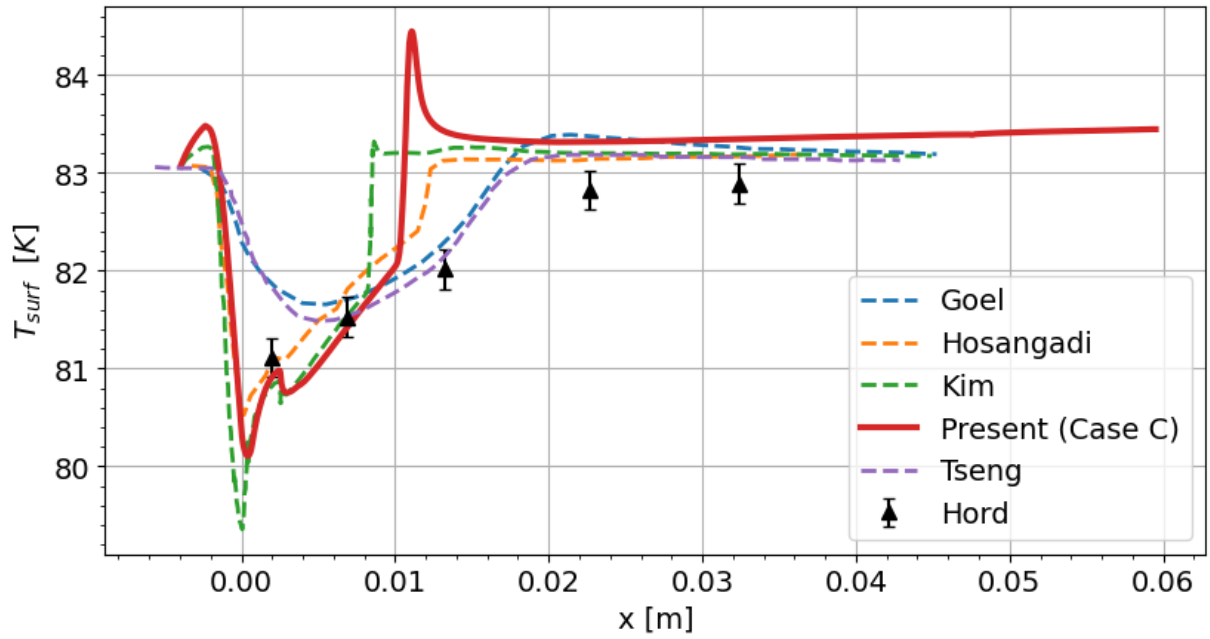


Figure 23: Surface temperature of Case C vs experiments and numerical results from Kim and other studies Goel [5], Tseng [32], Hosangadi [9]

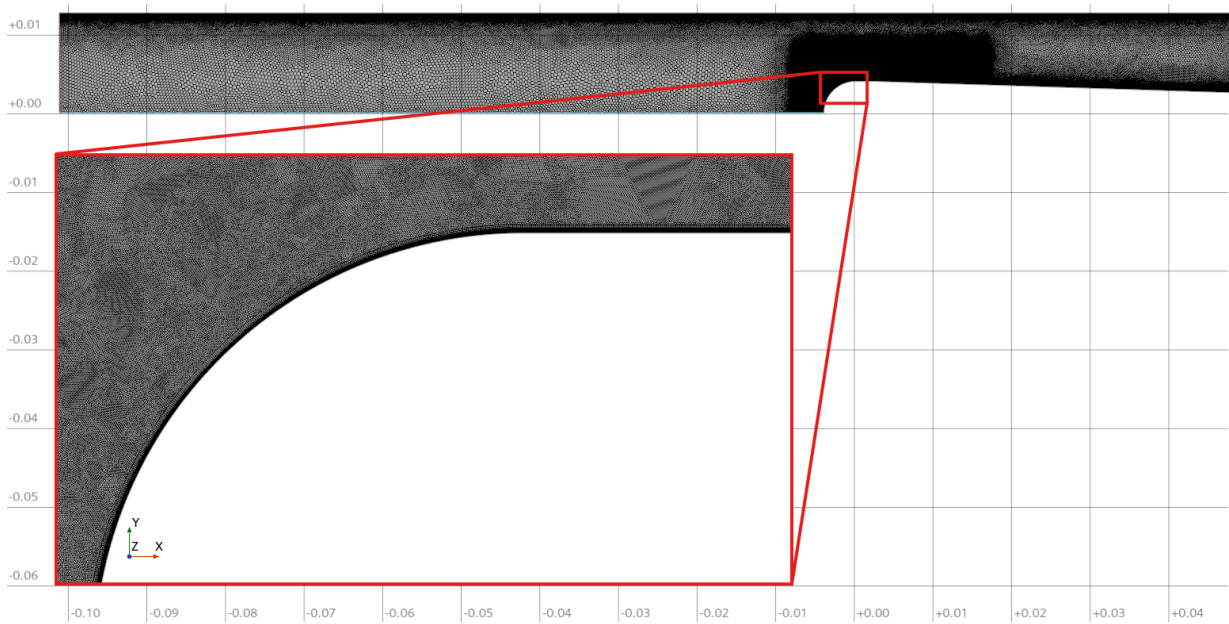


Figure 24: Refined 2d mesh with detailed view

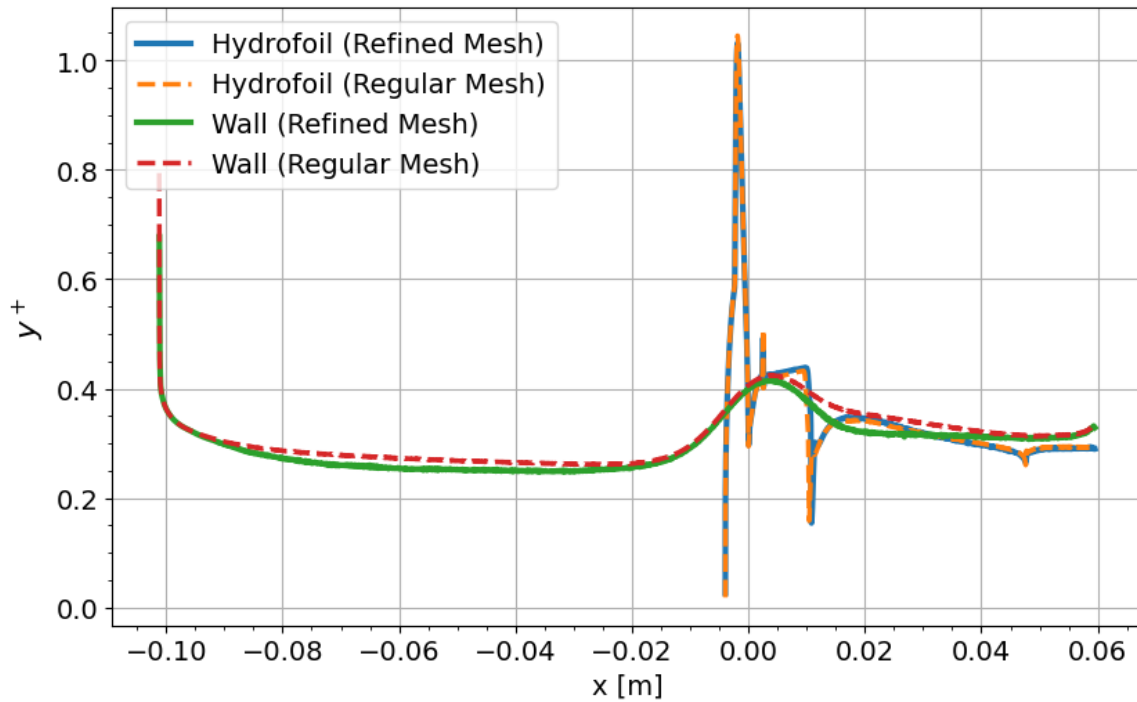


Figure 25: y^+ along walls for both meshes

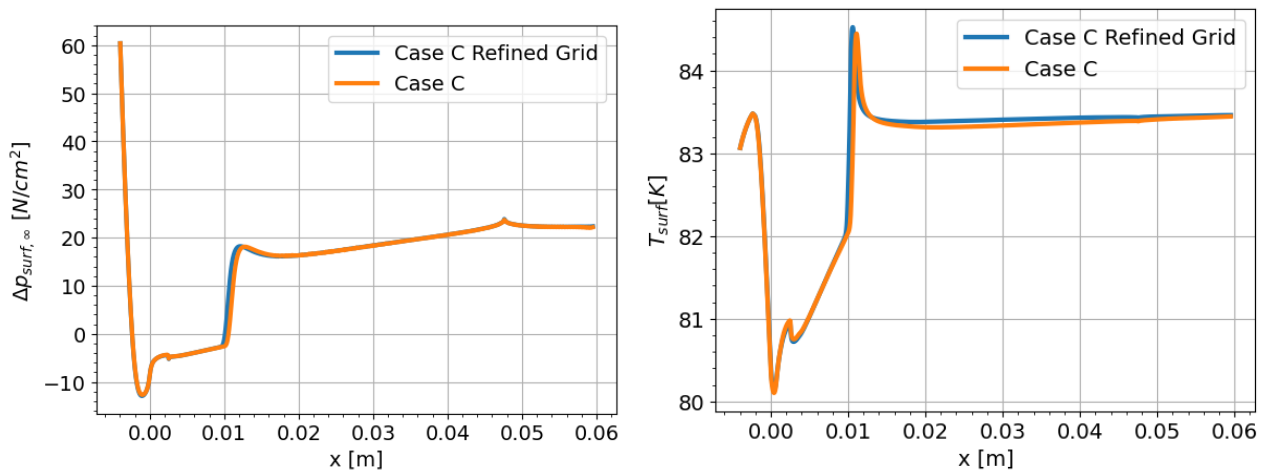


Figure 26: Surface pressure depression and temperature for case C with regular and refined mesh

Parameter	Value
Number of cells	3667949
Base size	0.0025m m
Target size	$7.5 \cdot 10^{-4}$ m (30%)
Minimum cell size	$1.25 \cdot 10^{-4}$ m (5%)
Growth rate	1.2
Prism layer total thickness	$1 \cdot 10^{-4}$
Layer near wall thickness	$1 \cdot 10^{-7}$ m
Number of layers	30
Refinement box cell size	$6.25 \cdot 10^{-5}$ m (2.5%)

Table 9: Mesh setup parameters for 3d RANS simulations. Dimensions relative to base size between brackets ()

from all three directions contribute to transport, production and dissipation of turbulent quantities. Therefore it is logical to wonder if any information is lost when considering a 2d approximation. In this section 3d simulations are developed and run to investigate the presence of relevant effects due to the third dimension (along the span wise direction) being considered.

Realistic cavitating flows can be obtained only through LES turbulence modeling, while unsteady RANS such those employed until now are a useful method to solve the mean flow (thus fit for steady cavities) but scales of turbulence are completely smoothed out.

In this section no scale resolving model will be applied: instead, the same $k - \omega SST$ model will be employed to extend the problem to the third dimension as the main focus is verifying the presence of (possible) 3d effects.

4.4.1 Simulation setup

Simulating 3d flows is quite more expensive than 2d, due to the larger number of grid cells required to get the same mesh resolution. Given the limit on available computational resources, computing the full width tunnel was not a viable option without losing a fair amount of accuracy. For this reason just a slice of the domain (0.005 m wide) has been used to define the geometry and periodic interfaces have been imposed at the sides. Obviously, the span wise width had been chosen large enough so that dynamics in the z direction could take place.

All the other aspects of the simulation (i.e. fluid properties, solver settings and numerical schemes) are tuned according to the setup of case C defined in the previous section.

The geometry has been built by simply extruding 0.005 m in z direction the planar section from figure 5. No modifications has been made to the type of boundary conditions.

As anticipated, the sidewalls have been treated as periodic interfaces, such that whatever happens on one side is repeated on the other. In this way there's no need for mesh refinement along the z axis and the problem becomes equivalent to an indefinitely extended hydrofoil.

The mass flow rate to be set at the outlet changes accordingly to the new area of the inlet section:

$$\dot{m}_{in} = \dot{m}_{out} = v_{in} \cdot \rho_{in} \cdot A_{in} = 1.18 \frac{\text{kg}}{\text{s}} \quad (25)$$

The other quantities (imposed as inlet boundary conditions) are still the same defined by Hord for case 290C and summarized in table 6.

A volume mesh has been generated using parameters defined in table 9. A refinement box is placed in the same position used for the 2d mesh. Figure 27 shows a cut section of the grid along on the median x-y plane, a detailed visualization near the hydrofoil and a top view of the mesh (where the uniform grid size can be appreciated).

Unsteady behavior and turbulence viscosity scaling One aspect regarding cavity unsteadiness and RANS turbulence modeling applied to cavitating flows has been addressed by Reboud et al. [27]. More specifically, in this study the authors argue that models based on Boussinesque's approximation (specifically $k - \epsilon$) tend to overestimate the eddy viscosity in the cavity wake, which in turn results in stable cavities preventing the formation of re-entrances and shedding typical of separated flows break-off cycle (e.g. those of aerodynamic surfaces at high angle of attack).

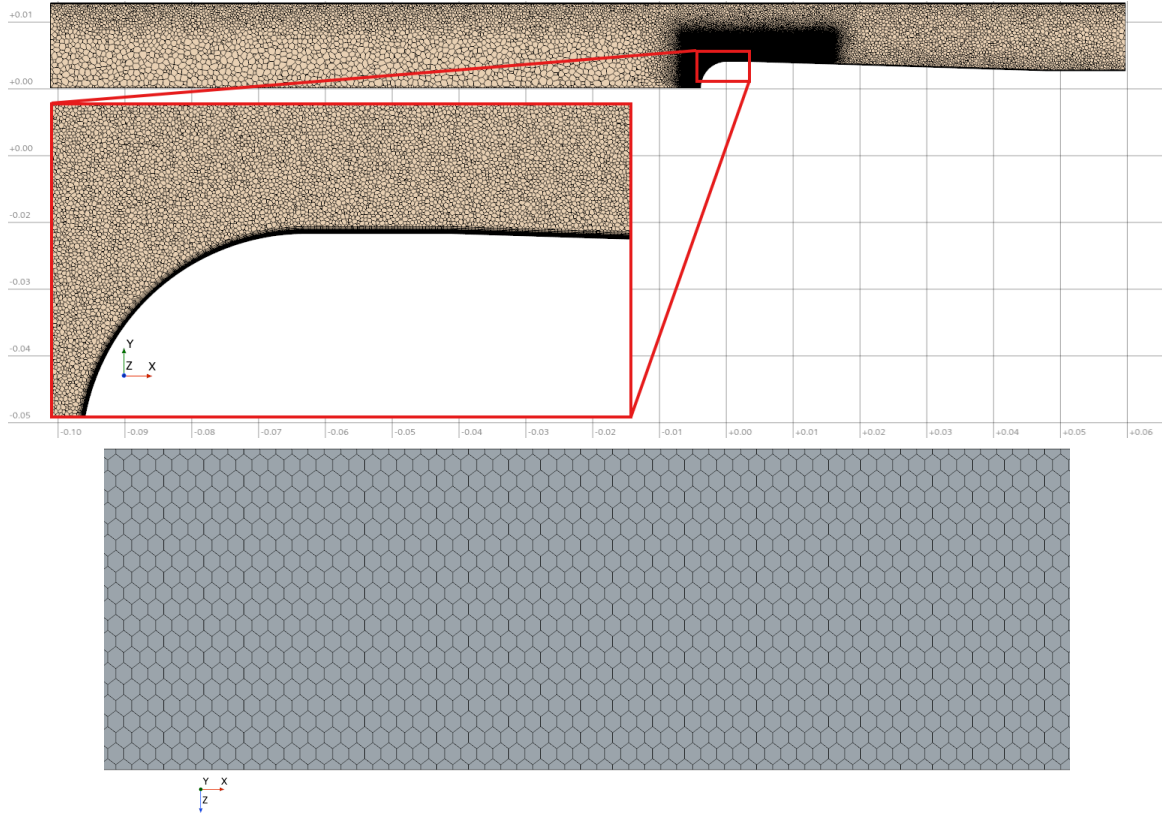


Figure 27: Cut plane (with detail) and top view of the 3d mesh

In order to circumvent this issue and avoid the necessity to resolve (at least some) scales of turbulence, Reboud came up with the idea of scaling the computed turbulent viscosity value as a function of the phase density. Basically, the scaling factor is lower than unity *inside* the cavity, while outside (i.e. in the liquid phase) it is regularly computed according $k - \omega$ SST model. The scaling factor or (Reboud Correction) is defined as:

$$f_R(\rho) = \frac{1}{\rho} \left[\rho_v + \frac{(\rho - \rho_v)^n}{(\rho_L - \rho_v)^{n-1}} \right] \quad (26)$$

with the constant n being equal to:

$$n = 10$$

Apparently this issues does not affect the cavitating flow of the present experiment, since the developed cavity is stable and should not be affected by any large scale unsteadiness (see also Hosangadi [9]). Nevertheless, the aforementioned study [27] reports that also stable cavities can benefit from the application of an eddy viscosity scaling. In this way, it is possible to capture slightly unsteady re-entrant jets of the cavity and in turn improve the results for surface pressure depression and temperature.

For this reason two simulations have been carried on, and their results will be compared in the following section:

- **Case D:** without eddy viscosity scaling
- **Case E:** with eddy viscosity scaling (Reboud correction)

The simulations for case E will be run for $7.62ms$ (about 2.7 flow through times), after which some statistics will be collected at each time step.

The fields of interest are pressure and temperature on the hydrofoil surface, as well as vapor volume fraction on the whole domain. Mean and variance of those fields have been monitored on a time step basis. For a generic field f and N samples at the i -th collection step:

$$MEAN(f) = \frac{1}{N} \sum_{i=1}^N f_i \quad (27)$$

$$VAR(f) = \frac{1}{N-1} \left[\sum_{i=1}^N f_i^2 - \frac{1}{N} \left(\sum_{i=1}^N f_i \right)^2 \right] \quad (28)$$

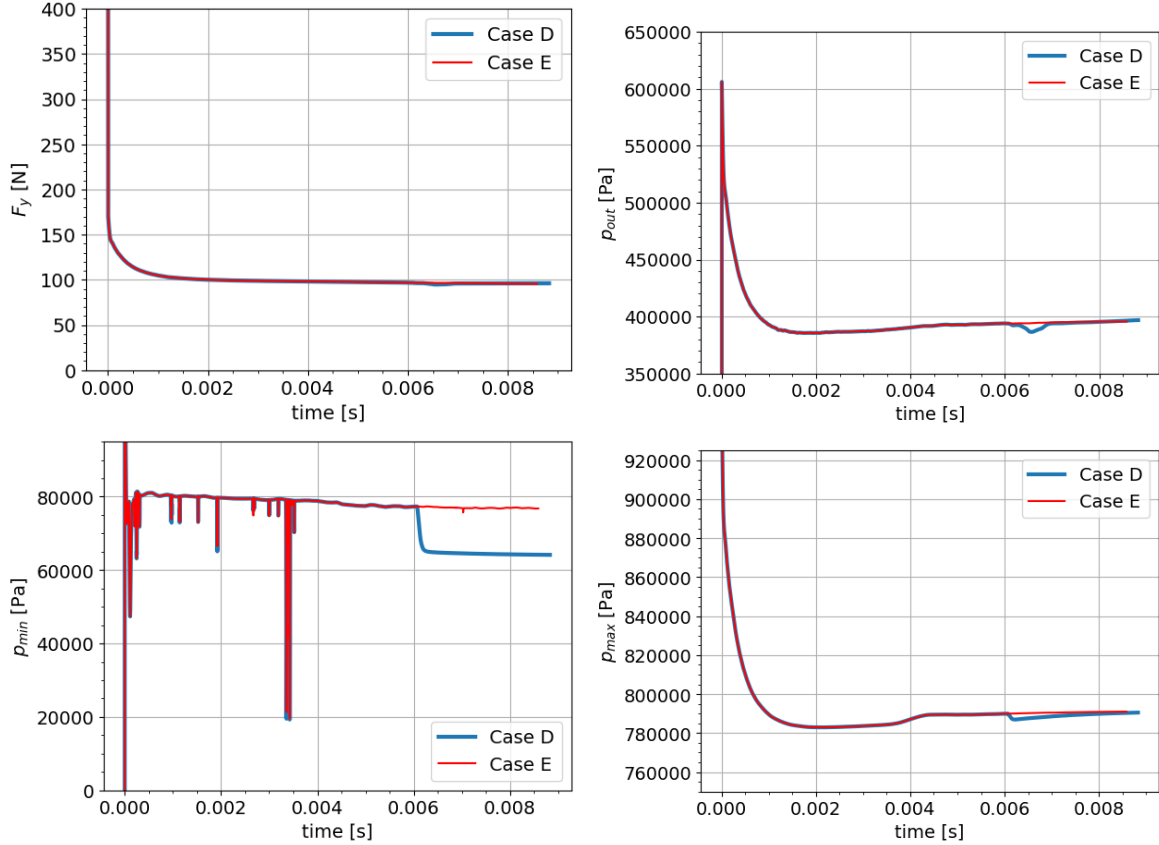


Figure 28: Monitored quantities

Initial conditions Case E has been initialized using solution interpolation from a 2d simulation (case C) in incipient cavitation conditions. Case D is initiated from case E after about 6 ms. This can also be seen from figure 28, where monitored quantities are plotted: the two data series are partially overlapped for this reason.

4.4.2 Results

Both simulation have been run for about 8.5 ms (or 3 flow through times). Several quantities have been monitored during the execution, to verify the correct convergence of global parameters such as the vertical force on the hydrofoil, the average value of outlet pressure and minimum/maximum pressure values. Figure 28 shows that all of those quantities reached some sort of asymptotic behavior.

In order to check the effectiveness of periodic interfaces, mass flow rate through both sides of the domain has been monitored. Then, they have been summed to compute the net value that should be null. Figure 29 reports that it has been found to be always way lower than machine epsilon.

Now the usual comparison with pressure and temperature measures is performed. This time, since the geometry is three dimensional, some sort of space averaging is needed. To do that, data on the hydrofoil surface are averaged along the z direction for a give set of intervals Δx . Moreover, case E requires also the fields to be time averaged in order to get meaningful results.

The other data used for plots in figures 30 and 31 are:

- Hord’s experimental measures
- 2d computation of case C exposed in the previous section
- two dataset provided by two different simulations performed by Kim[13]. The first one features the same Schnerr-Sauer model used in the present work; the other employs a cavitation model that accounts for the whole bubble growth regimes spectrum.
- Pressure and temperature values at the hydrofoil’s centerline (parallel to the stream-wise direction) for case D and E.

Figures 30 and 31 reveal that both cavities developing in 3d simulations are twice as long than those found in 2d computations. This result is unexpected, given that many models and configurations are shared with case C. Elongated cavities are often associated with thermal effects being the limiting factor for the bubble growth, but here it is clearly not the case. An important aspect to consider when evaluating these results is space discretization (i.e. computational grid). Due to limitation on computational resources, the 3d mesh has

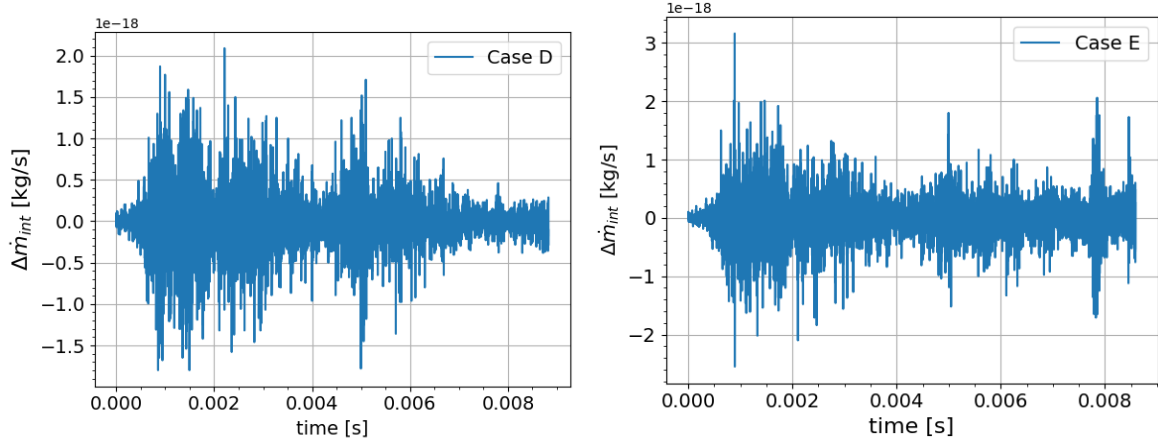


Figure 29: Net mass flow rate through interfaces

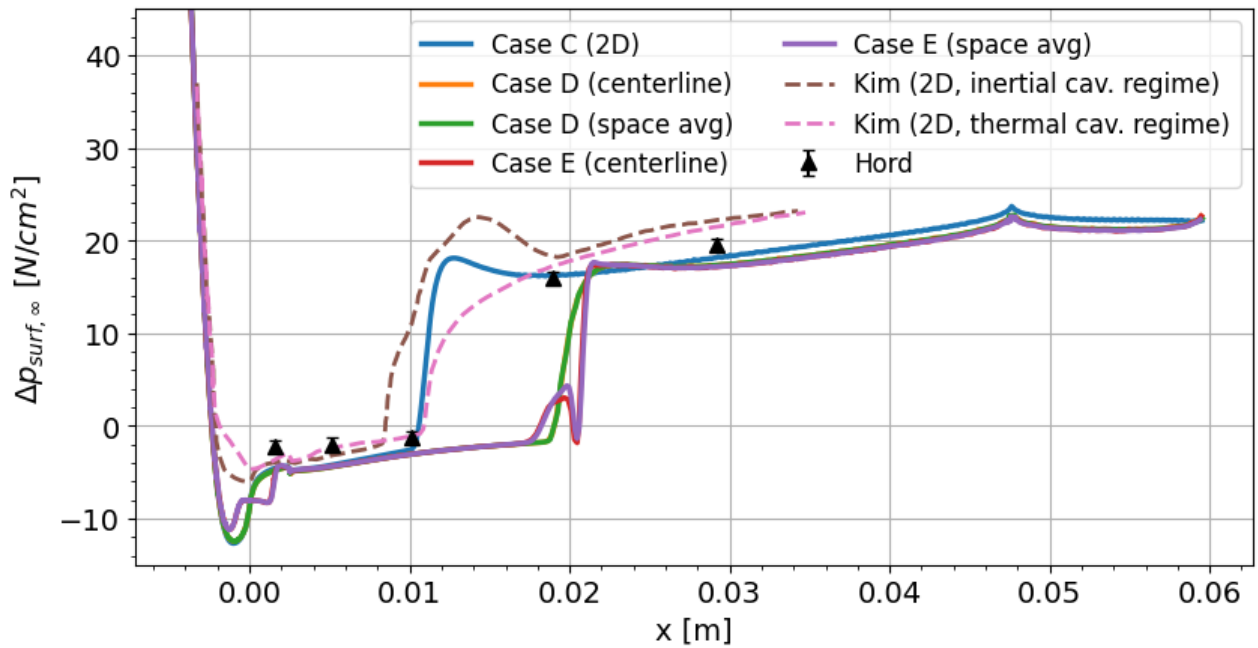


Figure 30: Surface pressure depression model comparison

a lower grid resolution than the 2d baseline mesh (values can be compared among table 8 and 9). In particular, for 3d mesh an higher value for cell size growth rate has been employed, making the grid outside the refined box much coarser. This can have a relevant impact on computation considering that the cavity extended beyond the refined region's limits, potentially decreasing the accuracy of computations in a delicate zone.

Some conclusion can be drawn by observing the two plots:

- spaced averaged and data from the hydrofoil's center line are not very far from each other. As a matter of fact, only for case E the two data series diverge in a confined region near the cavity's tail
- Case C, D and E have similar pressure distributions in the central region of the cavity, and they approximate experimental data fairly well.
- Near the leading edge, the hydrofoil experiences a more drastic temperature decrease with case E than in the other simulations.
- Case C can intersect within instrument tolerance all pressure data, but performs worse than both 3D cases and Kim's thermal model when temperature is considered.

Figures 33 and 32 show in more detail the difference among centerline and space averaged results. They are completely superimposed for case D, while case E exhibits a small deviation especially for temperature data. Since the difference among space-averaged and centerline data is small, a vertical plane intersecting the hydrofoil at the centerline (from now on, the *mid-plane*) can be effectively employed to show meaningful internal fields as done in figures 34, 35, 37, 36 and 38. They also contain the flow fields of case C for a broader comparison among different models of the same experiment.

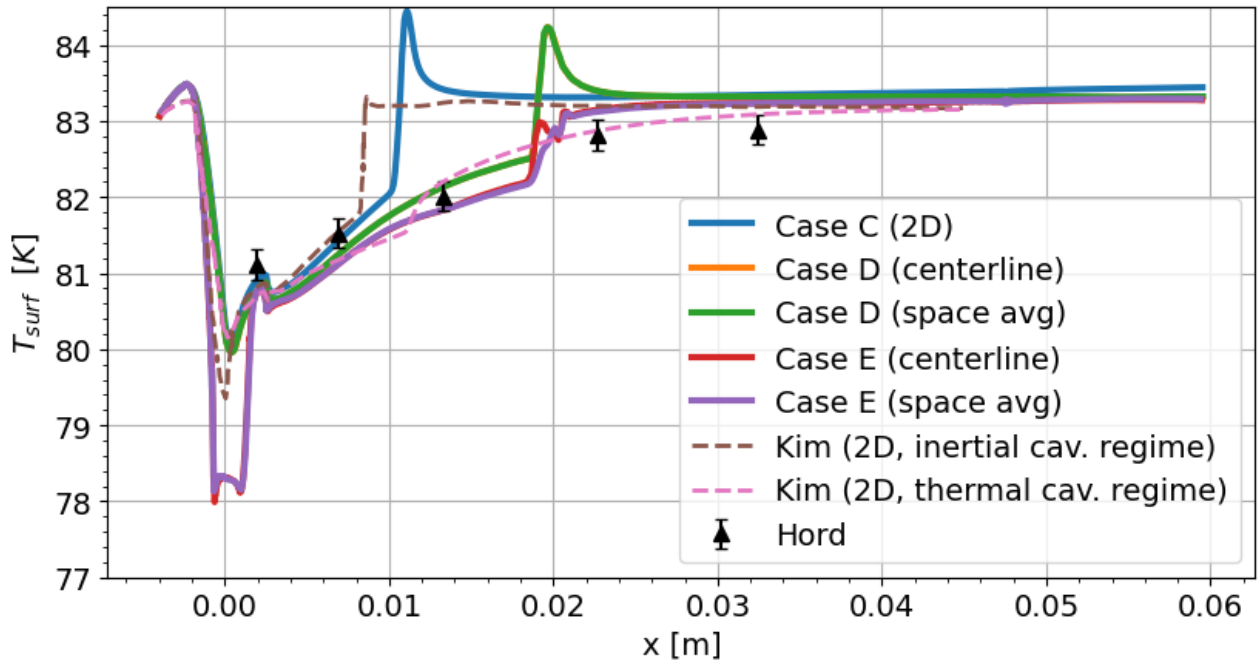


Figure 31: Surface temperature model comparison

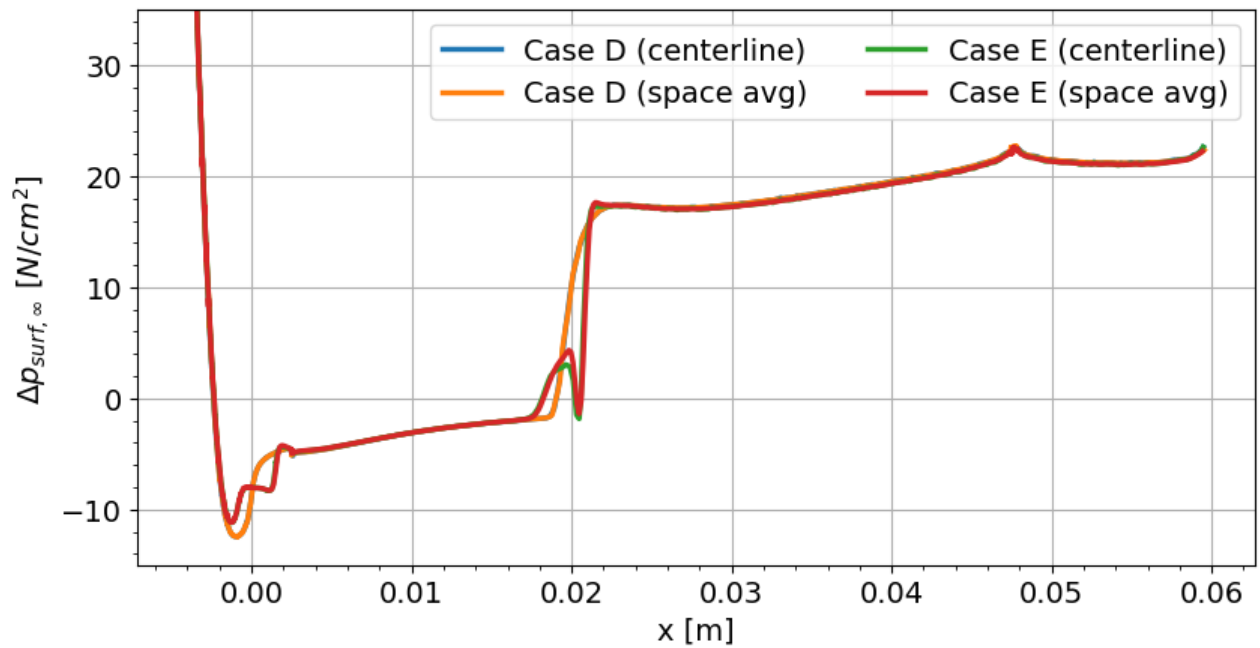


Figure 32: Surface pressure depression: comparison among space averaged and data on the mid-plane

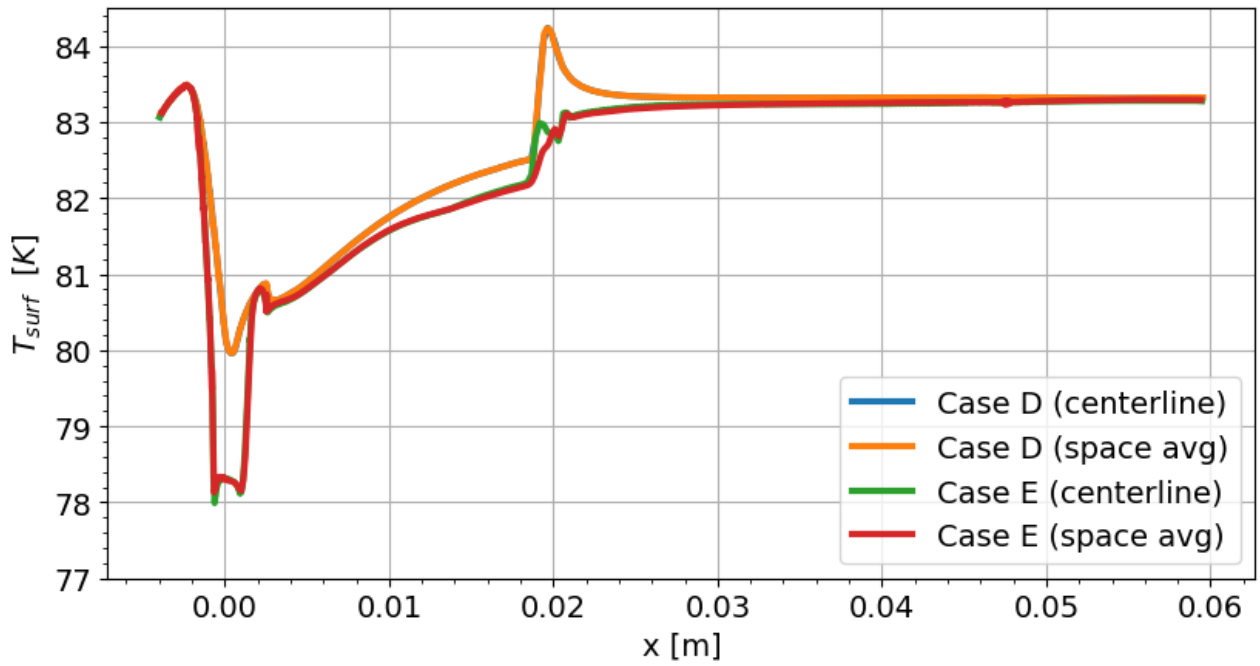


Figure 33: Surface temperature: comparison among space averaged and data on the mid-plane

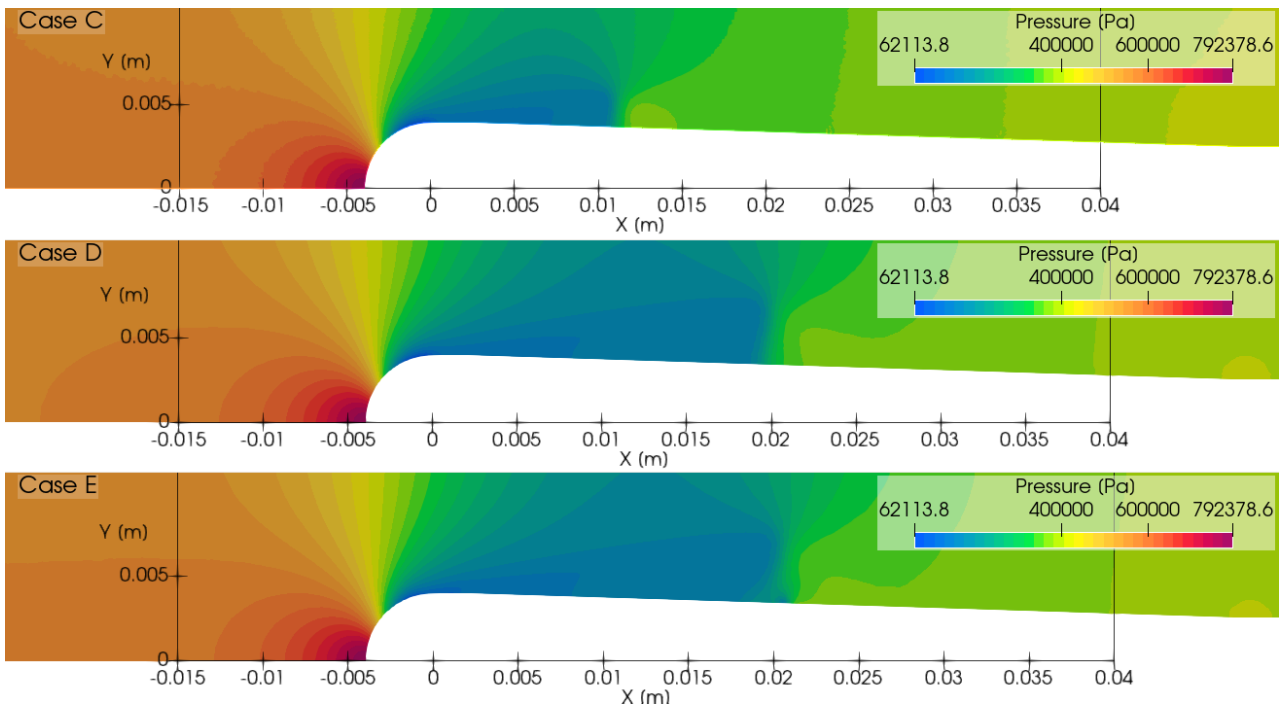


Figure 34: Mid-plane comparison of pressure field

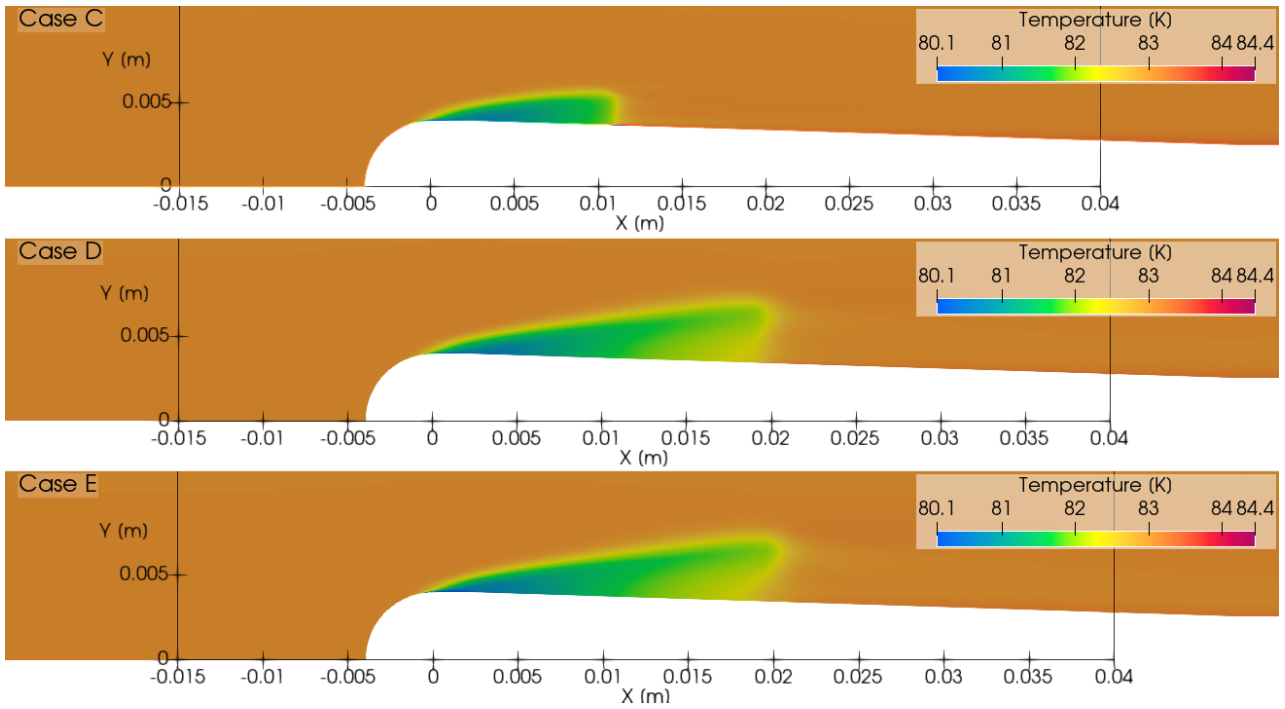


Figure 35: Mid-plane comparison of temperature field

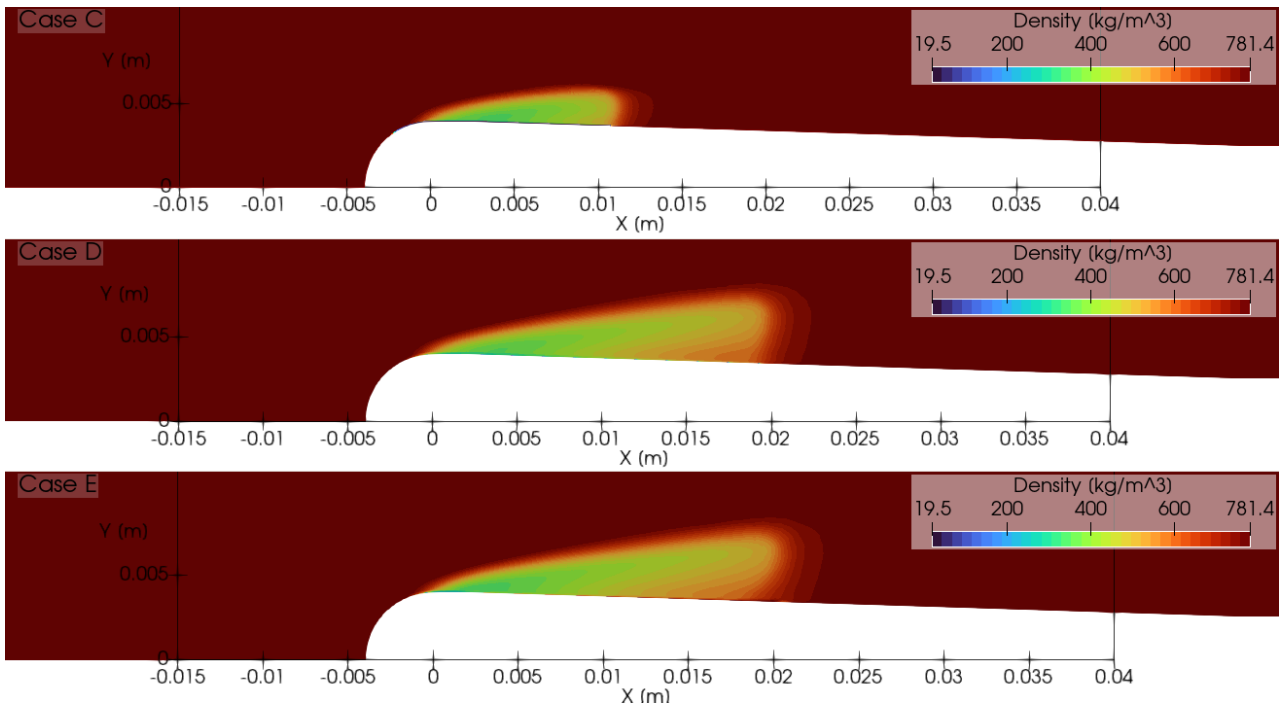


Figure 36: Mid-plane comparison of the density field

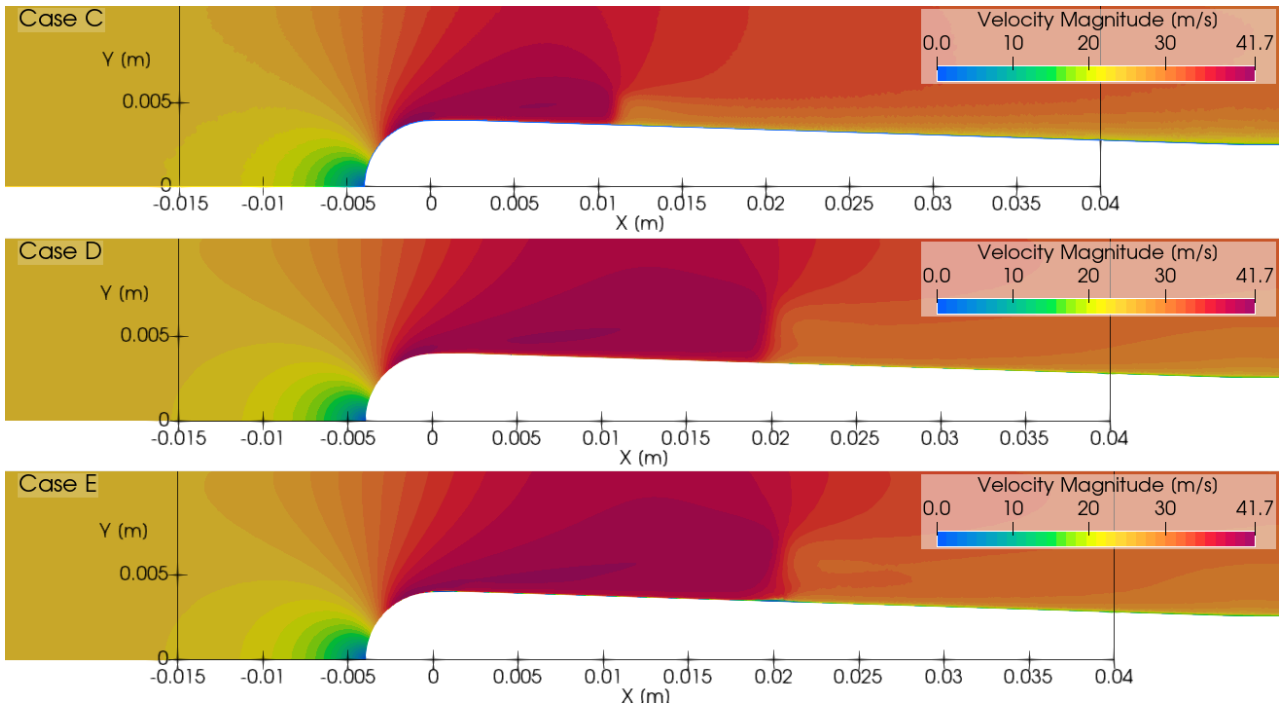


Figure 37: Mid-plane comparison of the velocity field

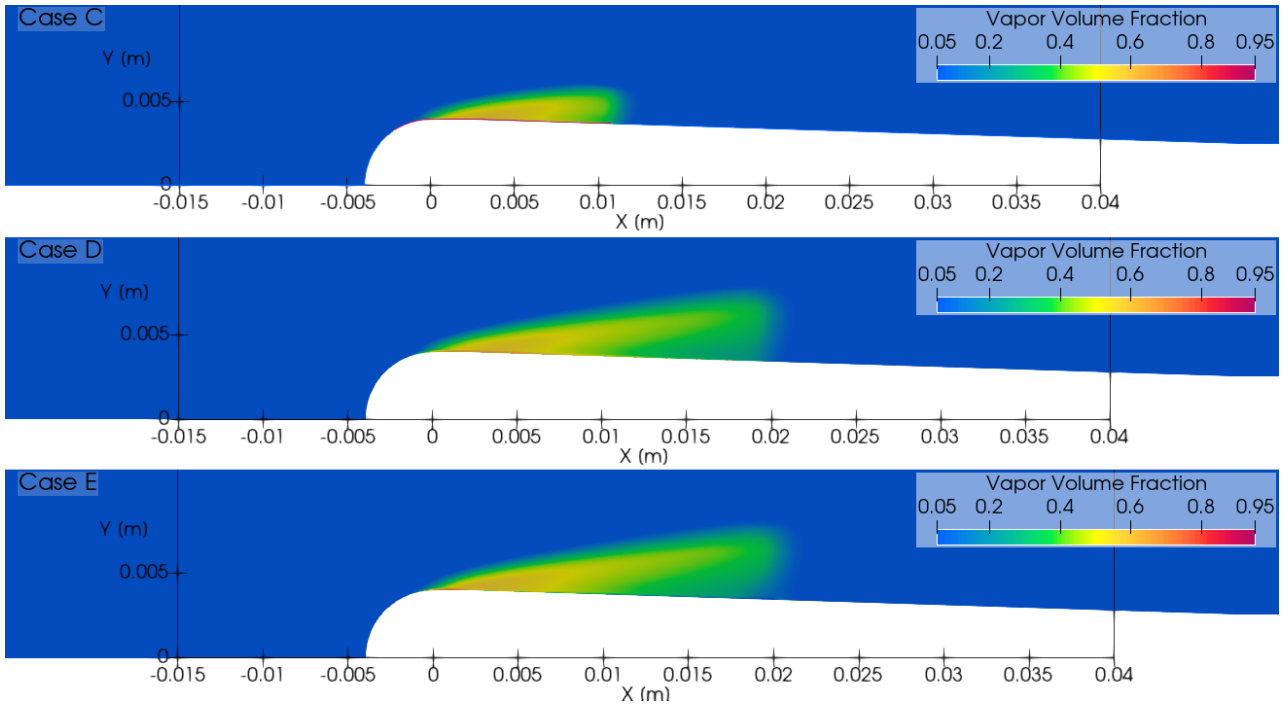


Figure 38: Vapor volume fraction on mid-plane

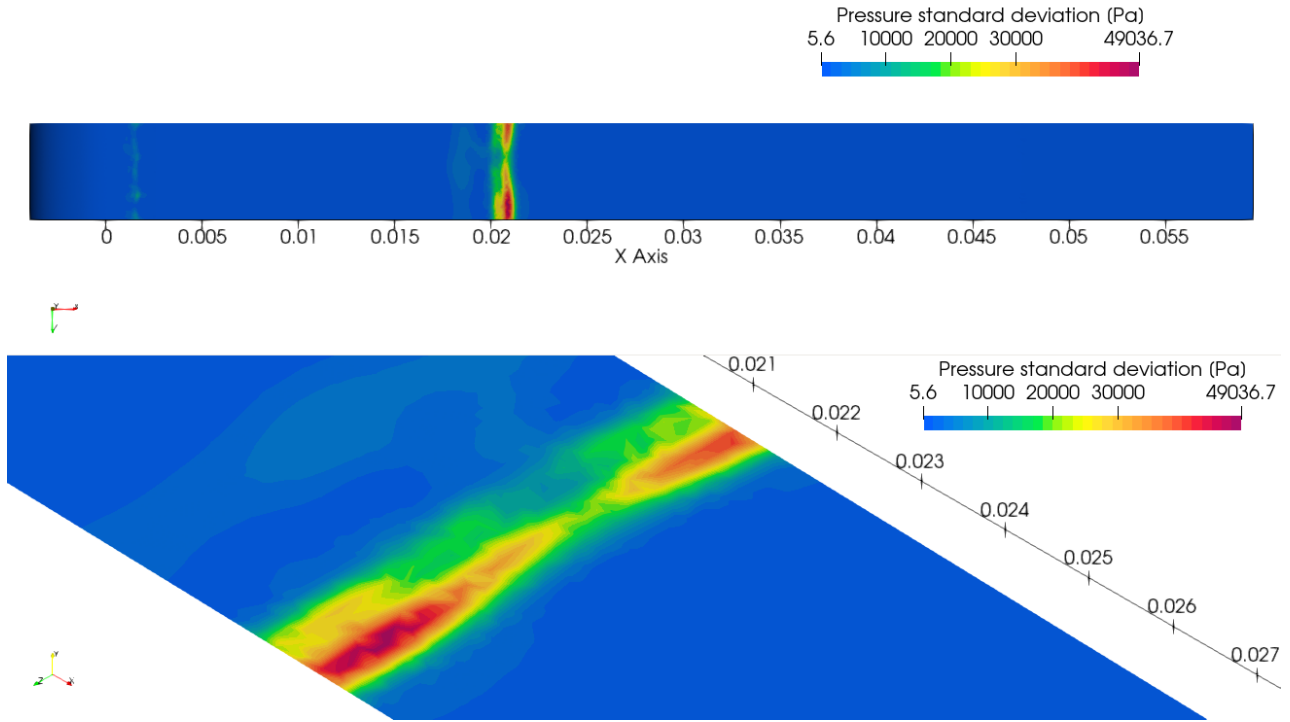


Figure 39: Standard deviation of surface pressure (case E)

The fields for vapor volume fraction in figure 38 confirm the hypothesis of longer cavities being developed in 3d simulations. For both case D and E the cavity length is quite close to the value of 19 mm measured by Hord. For case E, temporal mean and variance of pressure and temperature have been computed in each cell over the span of about 1 ms. As the main concerns are surface pressure depression and surface temperature, only statistics over the hydrofoil's surface have been collected. Figure 39 and 40 depict the heatmap of standard deviation on the hydrofoil surface. From these pictures it is possible to identify clearly two area where unsteady phenomena are stronger, which are the cavity tail and the area near the peak of pressure depression. The first is interested by both temperature and pressure unsteadiness, while for the leading edge only temperature is relevant as much as it is in the cavity tail. One interesting aspect to note is that the distribution of variance along the span-wise direction is non uniform, hence it may suggest the presence of three dimensional effects. A brief analysis on a probabilistic basis has been performed. Figure 41 shows the probability density function for standard deviation of pressure and temperature on the hydrofoil surface. Logarithmic scale has been used to enhance the readability of the plot for pressure standard deviation, as it features rare events that exhibit large magnitudes up to 50 kPa (e.g. regions with high condensation rates).

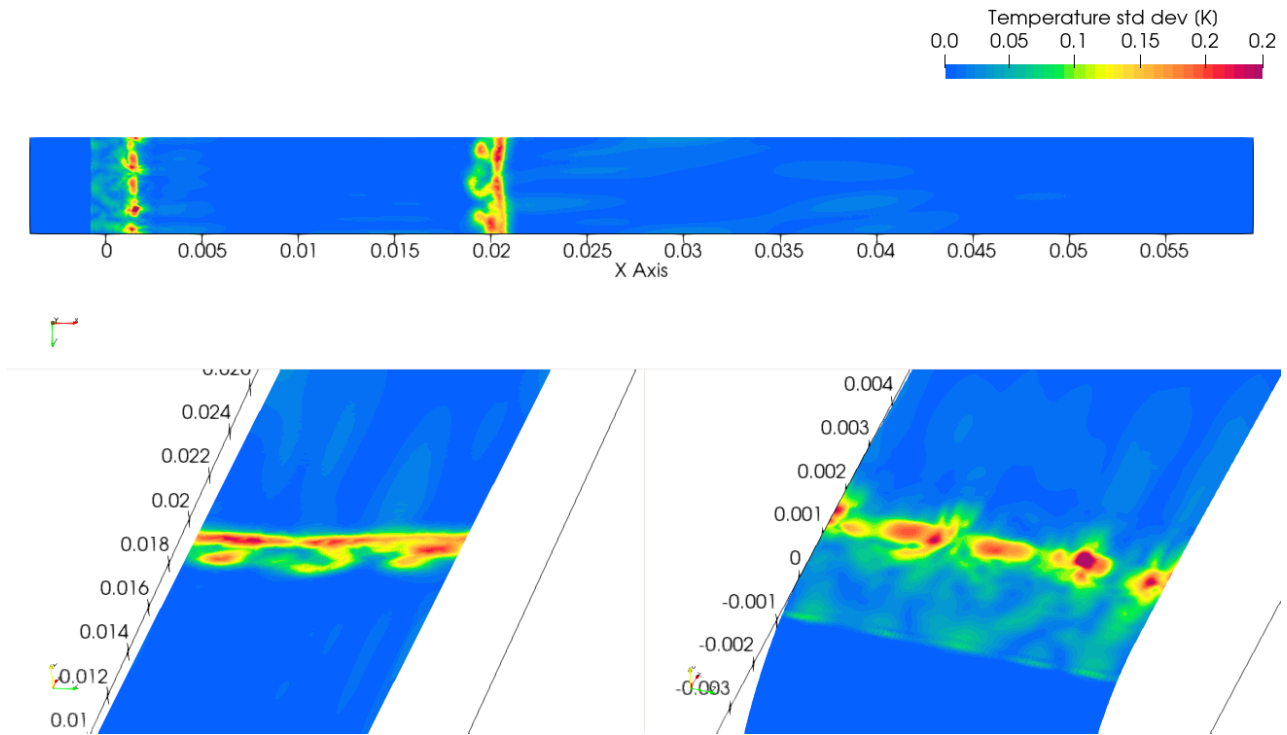


Figure 40: Standard deviation of surface temperature for (case E). Bottom left: cavity tail area. Bottom right: leading edge area.

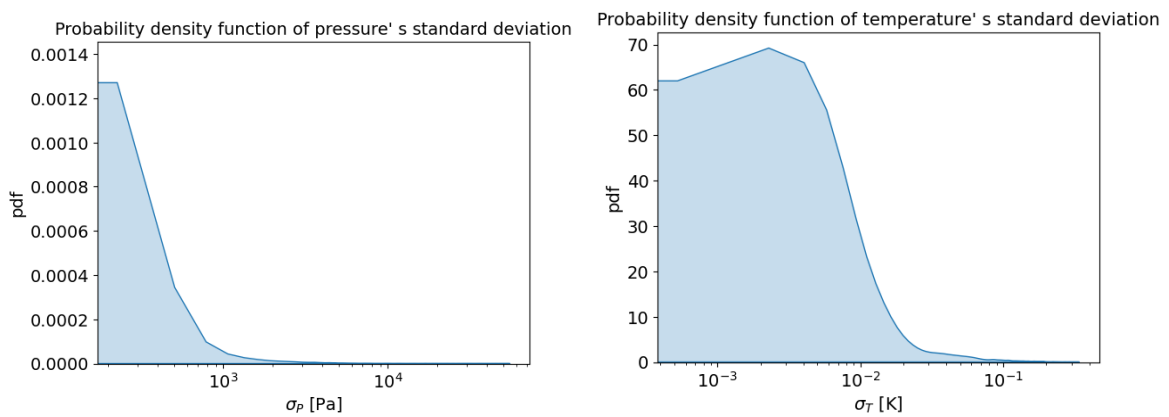


Figure 41: Probability density function of pressure (left) and temperature (right) surface standard deviation

5. Conclusions and possible future developments

In the present report a well established experiment has been analyzed and modeled in order to be able to perform numerical simulations that could be compared to experimental evidences. Countless studies regarding validation through Hord experimental setup exist, as it has become a baseline reference to compare against any new cavitation model proposal.

Some of them have been mentioned here, for instance Kim[13] have overcome the hypothesis of inertial controlled growth rate and homogeneous bubble number density. Others like Hosangadi[9], Goel[5] and Tseng[32] have tuned empirical constants in order to get the right vaporization and condensation rate that produce optimal results on both surface temperature and surface pressure depression.

In the present work, an attempt has been made to replicate the results following the best practices present in literature and adapting them to the specific case of interest in Starccm+ code.

To summarize:

- three meshes (two 2D and one 3D) have been generated and used.
- three different setup for material properties have been tested.
- In an attempt to reduce the time step interval for time discretization, it was found that for $CFL < 0.5$ the compressible solver gives raise to numerical instability.
- It was found that 3D simulations with periodic interfaces develops longer cavities than 2D
- With the present 3D setup it has been possible to get closer to experimental measures and obtain a cavity length quite close to the real one. Of course, without any other quantitative information about the flow field, it is difficult to establish if the present vapor volume fraction is correctly predicted. Most likely this is not the case, as empirical observation shows that this kind of cavity develops in tapered shapes typical of thermal controlled growth rates that cannot be replicated when thermal effects in cavitation are neglected (see [13]).
- Finally, Reboud correction have been successfully adopted for a problem that does not suffer separation or similar issues. Nevertheless this helped to identify unsteadiness in the mean field most probably suppressed regular RANS models are used.

The last point leads to the most natural evolution step for this kind of physical problem, which is scale resolving turbulence by means of LES or DES formulation. Performing these kind of computations require a large amount memory and cpu power, given the dimension for meshes needed to solve for the energy containing scales of turbulence. The advantage is that with LES/DES simulation it can be establish whether the predictions gained with the Reboud correction are correct or not. Given the concerns about the employed computational grid previously exposed, these results should be critically assessed checking actual mesh convergence before reaching final conclusions.

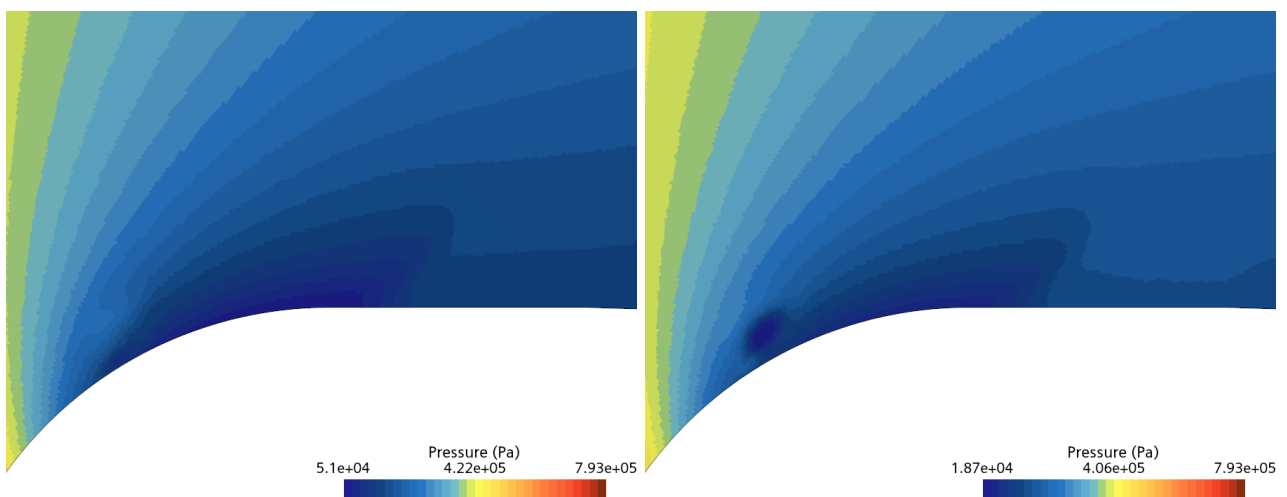
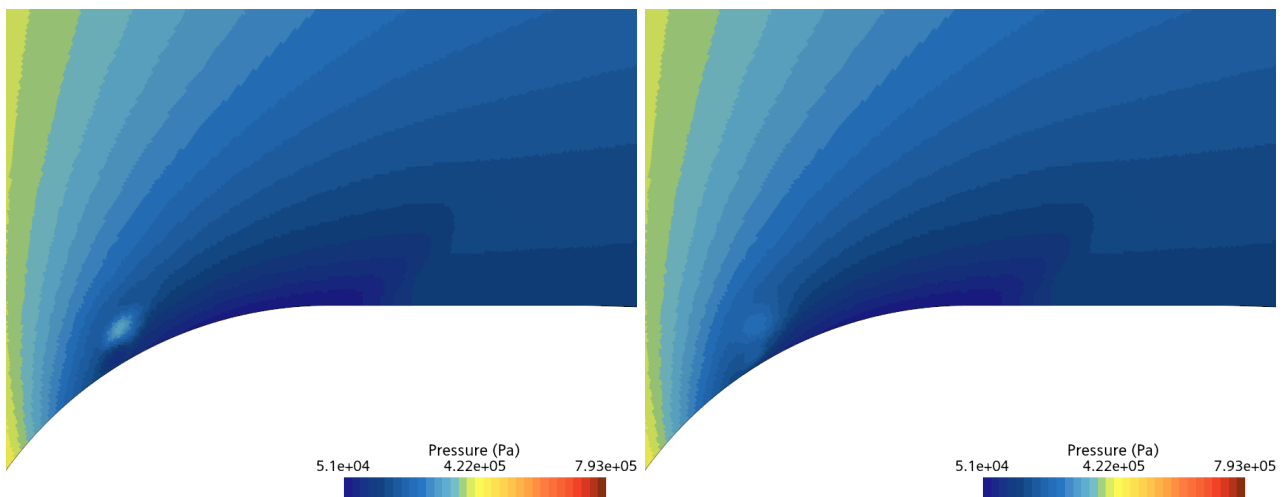
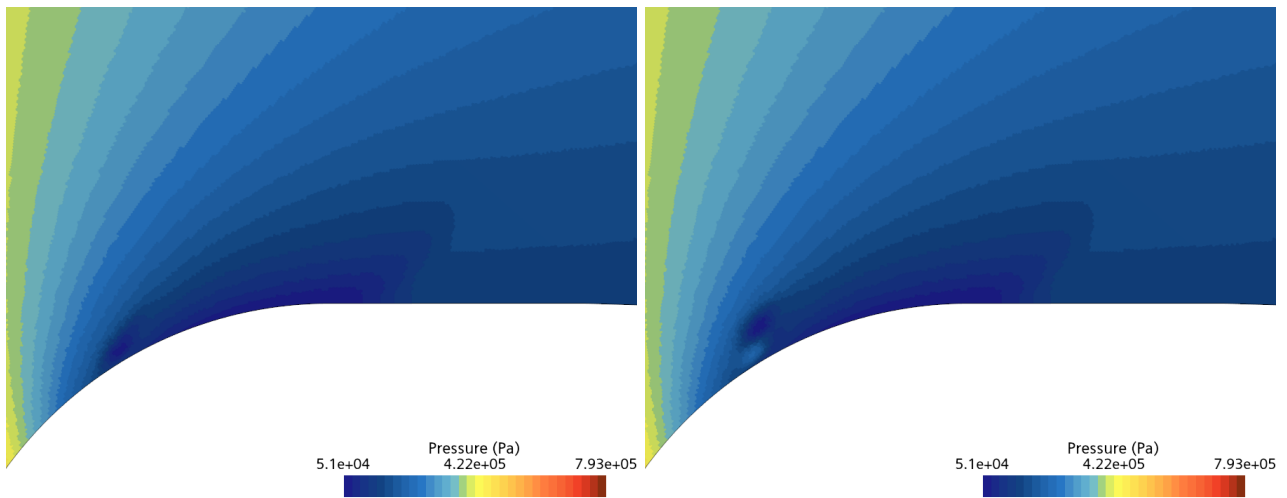
Finally, thermal effects need to be mentioned again. As already stated, they have been neglected all along while actually cavitation of cryogenes is dominated by thermal diffusion. For this reason, implementing a thermal growth model could help computing more appropriate pressure, temperature and vapor volume fraction fields. Kim [13] proposed a model based on Labuntsov's equation[15] and a variable seed density distribution based on probabilistic considerations and experimental results by De Giorgi et al.[4]. An alternative is offered by empirical models which require tuning constants for the vapor volume fraction's equation source term (e.g. ZGB cavitation model[34]) as performed for instance by Liu et al.[17]. In both cases, the formulation needs to be adapted to Starccm+ as convergence is not granted and may need to be improved. This might require an higher mesh resolution, different settings parameters (e.g. R_0 , η , relaxation factors) or using different solving algorithms (PISO instead of implicit SIMPLE). Extra attention needs to be payed when computing seed diameter using Kim's model: the value needs to be upper-bound in order to keep it from growing indefinitely. Negative values also need to be prevented, as in the original model there's no clear countermeasure to avoid it.

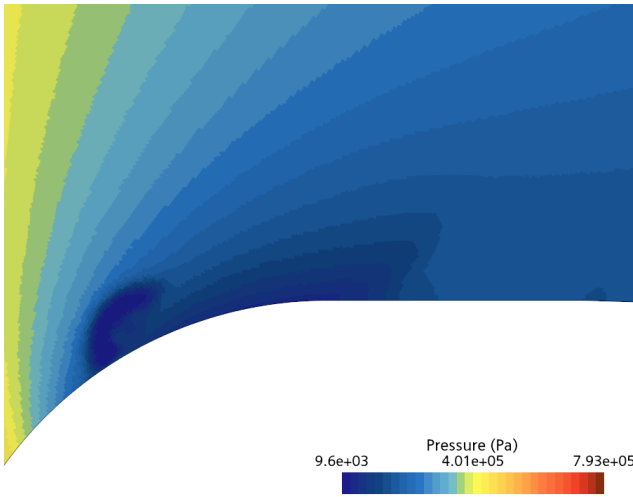
References

- [1] Ian H. Bell, Jorrit Wronski, Sylvain Quoilin, and Vincent Lemort. Pure and pseudo-pure fluid thermo-physical property evaluation and the open-source thermophysical property library coolprop. *Industrial & Engineering Chemistry Research*, 53(6):2498–2508, 2014.
- [2] Christopher Brennen. Cavitation and bubble dynamics. *Cavitation and Bubble Dynamics*, 44, 01 1995.
- [3] J.H. Ferziger, M. Perić, and R.L. Street. *Computational Methods for Fluid Dynamics*. Springer International Publishing, 2019.
- [4] Maria Grazia De Giorgi, Antonio Ficarella, and Donato Fontanarosa. Numerical investigation of non-isothermal cavitating flows on hydrofoils by means of an extended schnerr–sauer model coupled with a nucleation model. *Journal of Engineering for Gas Turbines and Power*, 2020.
- [5] Tushar Goel, Siddharth Thakur, Raphael T. Haftka, Wei Shyy, and Jinhui Zhao. Surrogate model-based strategy for cryogenic cavitation model validation and sensitivity evaluation. *International Journal for Numerical Methods in Fluids*, 58(9):969–1007, 2008.
- [6] C.W Hirt and B.D Nichols. Volume of fluid (vof) method for the dynamics of free boundaries. *Journal of Computational Physics*, 39(1):201–225, 1981.
- [7] Jesse Hord. Cavitation in liquid cryogenes. 2: Hydrofoil. 1973.
- [8] Jesse Hord, L. M. Anderson, and W. J. Hall. Cavitation in liquid cryogenes. 1: Venturi. 1972.
- [9] Ashvin Hosangadi and Vineet Ahuja. Numerical study of cavitation in cryogenic fluids. *Journal of Fluids Engineering-transactions of The Asme*, 127:267–281, 2005.
- [10] Theodore Katsanis and W. D. Mc Nally. Fortran program for calculating velocities and streamlines on a blade-to-blade stream surface of a tandem blade turbomachine. 1969.
- [11] Theodore Katsanis and W. D. Mc Nally. Fortran program for calculating velocities in a magnified region on a blade to blade stream surface of a turbomachine. 1969.
- [12] Hyunji Kim, Yohan Choe, D. Min, and Chongam Kim. Methods for compressible multiphase flows and their applications. *Shock Waves*, 29, 01 2019.
- [13] Hyunji Kim and Chongam Kim. A physics-based cavitation model ranging from inertial to thermal regimes. *International Journal of Heat and Mass Transfer*, 181:121991, 2021.
- [14] P.G. Kosky. Bubble growth measurements in uniformly superheated liquids. *Chemical Engineering Science*, 23(7):695–706, 1968.
- [15] D.A. Labuntsov, V.A. Kol’chugin, and V.S. Golovin. The study of bubble growth under the boiling of saturated water in a wide range of pressure changes with the help of rapid filming. *Teplofiz. Vys. Temp.*, 2(3):446 – 453, 1964. Cited by: 75.
- [16] Ho Sung Lee and Herman Merte. Spherical vapor bubble growth in uniformly superheated liquids. *International Journal of Heat and Mass Transfer*, 39(12):2427–2447, 1996.
- [17] Wenguang Li, Zhibin Yu, and Sambhaji Kadam. An improved cavitation model with thermodynamic effect and multiple cavitation regimes. *International Journal of Heat and Mass Transfer*, 205:123854, 2023.
- [18] Yeong-Cheng Lien. Bubble growth rates at reduced pressure. 08 2005.
- [19] Adam D. Maxwell, Tzu-Yin Wang, Charles A. Cain, J. Brian Fowlkes, Oleg A. Sapozhnikov, Michael R. Bailey, and Zhen Xu. Cavitation clouds created by shock scattering from bubbles during histotripsy. *The Journal of the Acoustical Society of America*, 130(4):1888–1898, 10 2011.
- [20] B.B Mikic, W.M Rohsenow, and P Griffith. On bubble growth rates. *International Journal of Heat and Mass Transfer*, 13(4):657–666, 1970.
- [21] B. D. Nichols and Cyril W. Hirt. Methods for calculating multi-dimensional, transient free surface flows past bodies. 1975.

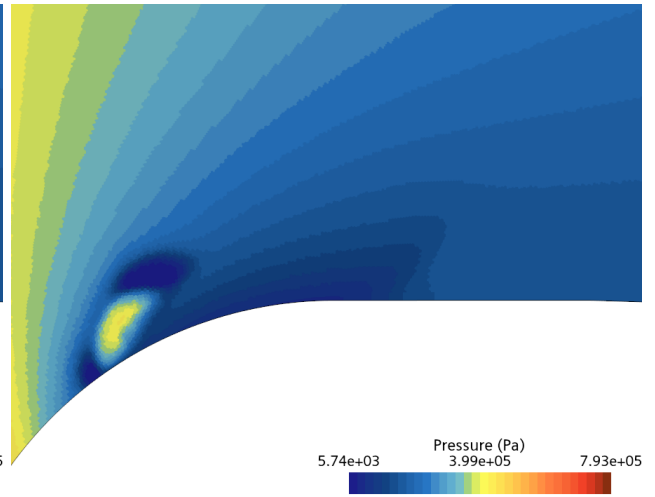
- [22] M. Peric. Using simulation to predict cavitating flow. 2021.
- [23] M. S. Plesset and S. A. Zwick. The Growth of Vapor Bubbles in Superheated Liquids. *Journal of Applied Physics*, 25(4):493–500, 04 1954.
- [24] Milton S. Plesset. The dynamics of cavitation bubbles. 1949.
- [25] Stephen B. Pope. *Turbulent Flows*. Cambridge University Press, 2000.
- [26] Lord Rayleigh. Viii. on the pressure developed in a liquid during the collapse of a spherical cavity. *Philosophical Magazine Series 1*, 34:94–98, 1917.
- [27] J. L. Reboud, Benoit Stutz, and Olivier Coutier. Two-phase flow structure of cavitation : Experiment and modelling of unsteady effects. 1998.
- [28] J. Sauer and Günter Schnerr Professor Dr.-Ing.habil. Unsteady cavitating flow - a new cavitation model based on a modified front capturing method and bubble dynamics. *Proceedings of 2000 ASME Fluid Engineering Summer Conference*, 251:1073–1079, 01 2000.
- [29] Jürgen S. Sauer. Instationär kavitierende strömungen - ein neues modell, basierend auf front capturing (vof) und blasendynamik [online]. 2000.
- [30] Siemens Digital Industries Software. Simcenter STAR-CCM+ User Guide v. 2021.1, Siemens 2021.
- [31] Siemens Digital Industries Software. Simcenter STAR-CCM+, version 2024.1, Siemens 2024.
- [32] Chien-Chou Tseng and Wei Shyy. Modeling for isothermal and cryogenic cavitation. *International Journal of Heat and Mass Transfer*, 53(1):513–525, 2010.
- [33] B. Yin, S. Yu, H. Jia, and J. Yu. Numerical research of diesel spray and atomization coupled cavitation by large eddy simulation (les) under high injection pressure. *International Journal of Heat and Fluid Flow*, 59:1–9, 2016.
- [34] Philip J Zwart, Andrew G Gerber, Thabet Belamri, et al. A two-phase flow model for predicting cavitation dynamics. In *Fifth international conference on multiphase flow*, volume 152. Yokohama Japan, 2004.

6. Appendix A: 2d compressible case with low CFL condition (0.3)

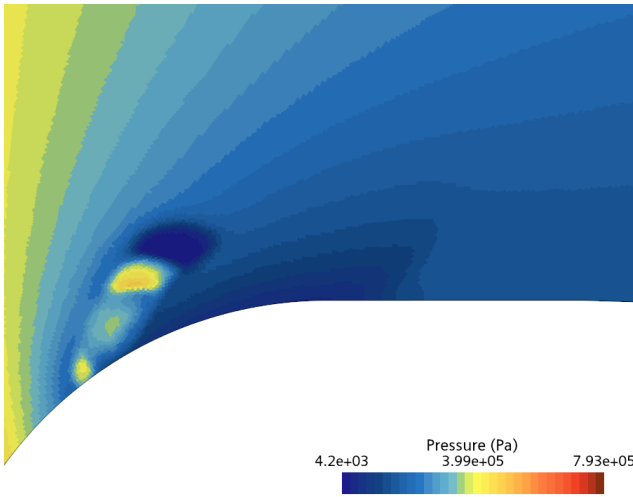




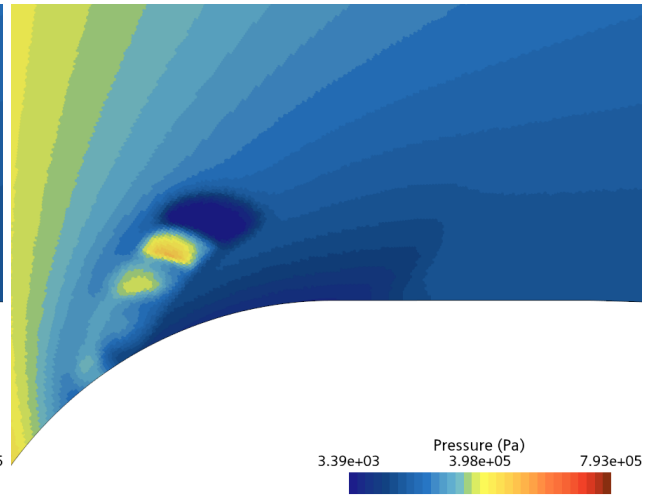
Solution Time 0.0200008 (s)



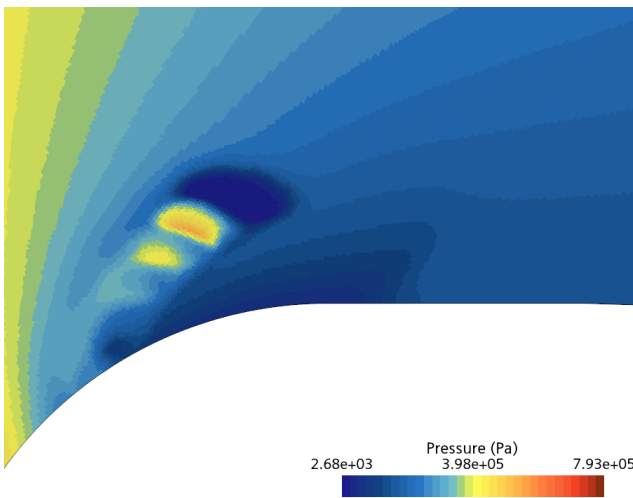
Solution Time 0.0200009 (s)



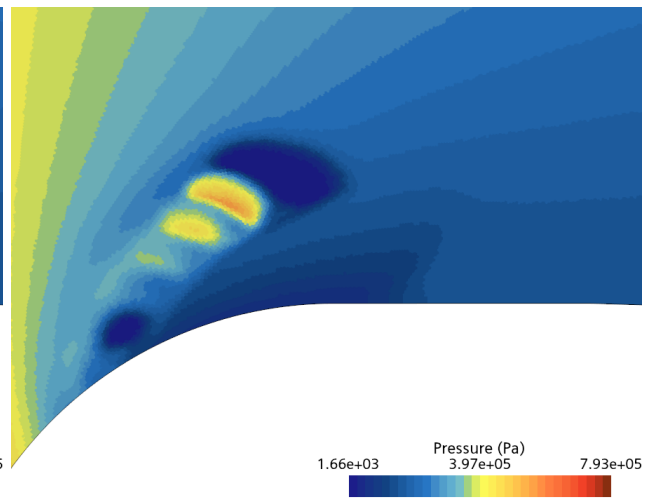
Solution Time 0.020001 (s)



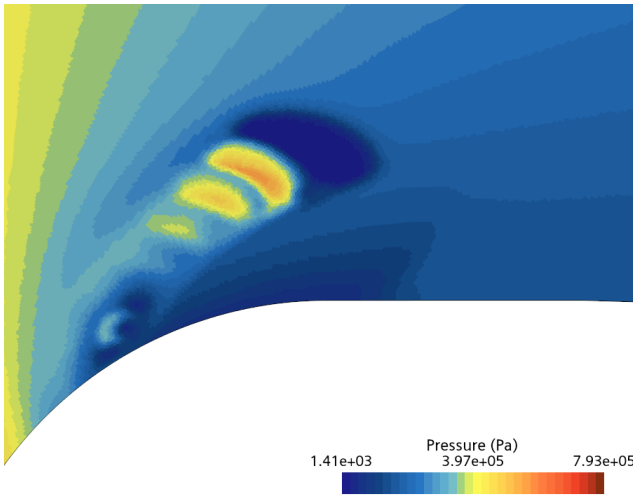
Solution Time 0.0200011 (s)



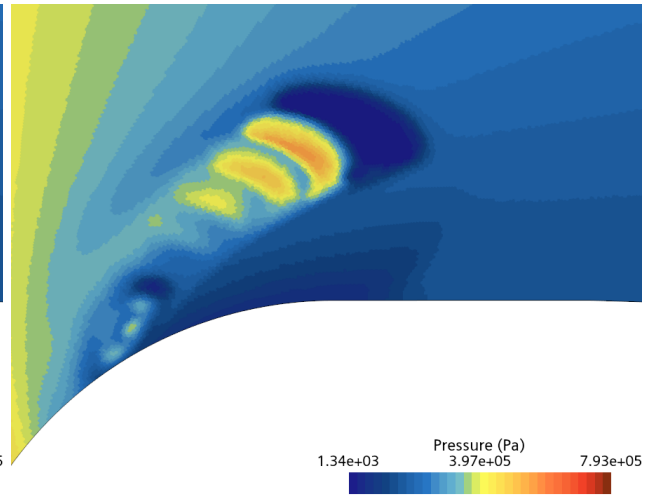
Solution Time 0.0200012 (s)



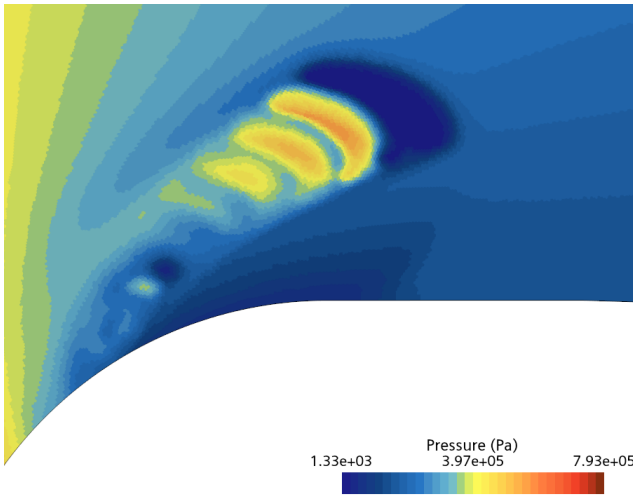
Solution Time 0.0200013 (s)



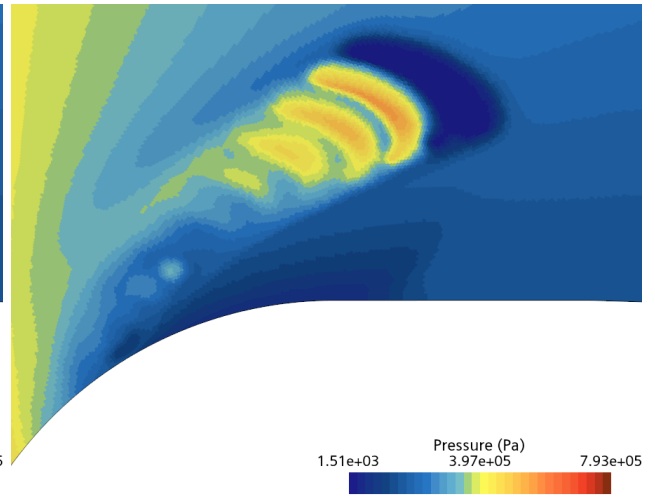
Solution Time 0.0200014 (s)



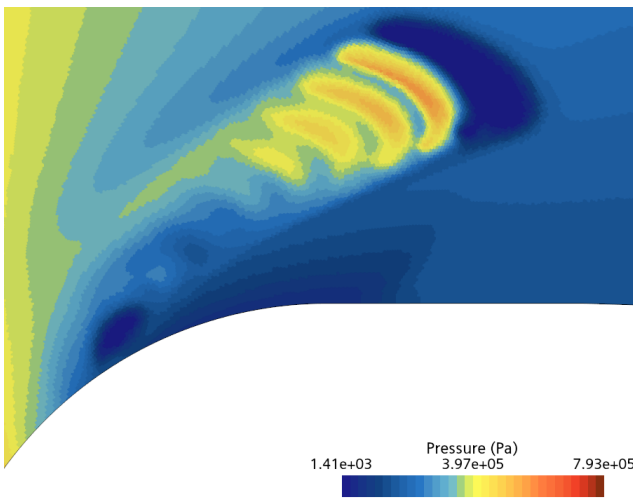
Solution Time 0.0200015 (s)



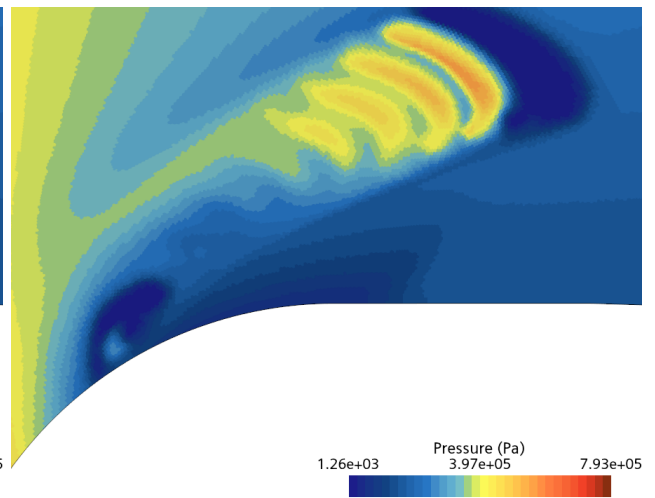
Solution Time 0.0200016 (s)



Solution Time 0.0200017 (s)



Solution Time 0.0200018 (s)



Solution Time 0.0200019 (s)

Abstract in lingua italiana

La cavitazione è un fenomeno complesso presente in molte correnti di interesse ingegneristico. Può rappresentare sia un rischio (es: Perdita di efficienza di una turbomacchina) sia un'opportunità (es: migliore atomizzazione degli iniettori di carburante).

Si tratta di un processo difficile da studiare sia sperimentalmente che numericamente: infatti è richiesta strumentazione molto avanzata e i modelli matematici sono comunque empirici. Ciò rende la validazione di qualsiasi risultato numerico obbligatorio tramite esperimenti.

In questo report, viene fatta una rapida introduzione teorica. Verrà usato il metodo di Schnerr-Sauer assieme alla tecnica VoF per risolvere il problema della cavitazione. Gli effetti termici non saranno considerati.

L'obiettivo è svolgere simulazioni CFD di un esperimento eseguito da Hord su di un profilo investito da una corrente di azoto liquido. L'attività è stata organizzata come segue.

Prima è stata considerata una corrente che non cavitava mono fase per validare la configurazione.

Poi è stata simulata una corrente 2D in cui avviene la cavitazione. È stato scoperto che usare una corrente comprimibile dà luogo ad instabilità numeriche se il CFL viene diminuito troppo. Pertanto sono state scelte proprietà dei fluidi incompressibili. I risultati sono stati confrontati con gli esperimenti ed altri studi numerici: non tenendo conto degli effetti termici nella fisica della cavitazione, l'estensione della cavità viene sottostimata nella simulazione.

Infine vengono svolte delle simulazioni 3D tenendo conto di una correzione alla viscosità turbolenta all'interno della cavità in modo da poter tener conto di eventuali effetti instazionari. I risultati ottenuti risultano più aderenti agli esperimenti rispetto a quelli delle simulazioni in 3d, inoltre riescono a calcolare correttamente la lunghezza della cavità

Parole chiave: Cavitazione; CFD; Starccm+; VoF; Flussi Multifase; Cavitazione a controllo inerziale

Acknowledgements

I want to thank my supervisors, prof. Federico Piscaglia, prof. Jens Honorè Walther and Nicolai Arent Quist for giving me the opportunity to join this project as well as for supporting me during the whole process. Their patience and precious advices have been very much appreciated.

I also want to express my gratitude to all my friends and my family, especially my parents who have always believed in me since forever and have been an invaluable and unconditional support and reference point.

This work is dedicated to my grandmother Lieta, who already knew I would make it.